



HAL
open science

Carbonated Inheritance in the Eastern Tibetan Lithospheric Mantle: Petrological Evidences and Geodynamic Implications

Fanny Goussin, Nicolas Riel, Carole Cordier, Stephane Guillot, Philippe Boulvais, Pierrick Roperch, Anne Replumaz, Karel Schulmann, Guillaume Dupont-Nivet, Filipe Rosas, et al.

► **To cite this version:**

Fanny Goussin, Nicolas Riel, Carole Cordier, Stephane Guillot, Philippe Boulvais, et al.. Carbonated Inheritance in the Eastern Tibetan Lithospheric Mantle: Petrological Evidences and Geodynamic Implications. *Geochemistry, Geophysics, Geosystems*, 2020, 21 (2), pp.e2019GC008495. 10.1029/2019GC008495 . insu-02498157

HAL Id: insu-02498157

<https://insu.hal.science/insu-02498157>

Submitted on 4 Mar 2020

HAL is a multi-disciplinary open access archive for the deposit and dissemination of scientific research documents, whether they are published or not. The documents may come from teaching and research institutions in France or abroad, or from public or private research centers.

L'archive ouverte pluridisciplinaire **HAL**, est destinée au dépôt et à la diffusion de documents scientifiques de niveau recherche, publiés ou non, émanant des établissements d'enseignement et de recherche français ou étrangers, des laboratoires publics ou privés.

RESEARCH ARTICLE

10.1029/2019GC008495

Special Section:

Tethyan dynamics: from rifting to collision

Key Points:

- Magmatic carbonates and mantle phlogopite have been found in 35 Ma lavas from Eastern Qiangtang
- H₂O-CO₂ metasomatism resulted in a very soft and fusible Tibetan subcontinental mantle lithosphere
- This allowed intracontinental subduction magmatism and accounts for the upper mantle low V_P anomaly

Supporting Information:

- Supporting Information S1

Correspondence to:

F. Goussin,
fanny.goussin@univ-grenoble-alpes.fr

Citation:

Goussin, F., Riel, N., Cordier, C., Guillot, S., Boulvais, P., Roperch, P., et al. (2020), Carbonated inheritance in the Eastern Tibetan lithospheric mantle: Petrological evidences and geodynamic implications. *Geochemistry, Geophysics, Geosystems*, 21, e2019GC008495. <https://doi.org/10.1029/2019GC008495>

Received 7 JUN 2019

Accepted 16 NOV 2019

Accepted article online 10 FEB 2020

Carbonated Inheritance in the Eastern Tibetan Lithospheric Mantle: Petrological Evidences and Geodynamic Implications

Fanny Goussin¹ , Nicolas Riel², Carole Cordier¹ , Stéphane Guillot¹, Philippe Boulvais³, Pierrick Roperch³, Anne Replumaz¹ , Karel Schulmann^{4,5}, Guillaume Dupont-Nivet^{3,6,8} , Filipe Rosas⁷ , and Zhaojie Guo⁸ 

¹Univ. Grenoble Alpes, University Savoie Mont Blanc, CNRS, IRD, IFSSTAR, ISTerre, Grenoble, France, ²Institut für Geowissenschaften, Johannes Gutenberg-Universität Mainz, Mainz, Germany, ³University of Rennes 1, CNRS, Geosciences, Rennes, France, ⁴University of Strasbourg, CNRS, EOST, Strasbourg, France, ⁵Center for Lithospheric Research, Czech Geological Survey, Prague, Czech Republic, ⁶Institut für Erd- und Umweltwissenschaften, Universität Potsdam, Potsdam, Germany, ⁷Instituto Dom Luiz, Faculdade de Ciências, Universidade de Lisboa, Lisboa, Portugal, ⁸Key Laboratory of Orogenic Belts and Crustal Evolution, Ministry of Education, Beijing, China

Abstract The timing and mechanism of formation of the Tibet Plateau remain elusive, and even the present-day structure of the Tibetan lithosphere is hardly resolved, due to conflicting interpretations of the geophysical data. We show here that significant advances in our understanding of this orogeny could be achieved through a better assessment of the composition and rheological properties of the deepest parts of the Tibetan lithosphere, leading in particular to a reinterpretation of the global tomographic cross sections. We report mantle phlogopite xenocrysts and carbonate-bearing ultramafic cumulates preserved in Eocene potassic rocks from the Eastern Qiangtang terrane, which provide evidence that the lithospheric mantle in Central Tibet was enriched in H₂O and CO₂ prior to the India-Asia collision. Rheological calculations and numerical modeling suggest that (1) such metasomatized mantle would have been significantly weaker than a normal mantle but buoyant enough to prevent its sinking into the deep mantle; (2) the slow seismic anomalies beneath Central Tibet may image a weakened lithosphere of normal thickness rather than a lithosphere thinned and heated by the convective removal of its lower part; and (3) melting of such soft and fusible metasomatized mantle would have been possible during intracontinental subduction, supporting a subduction origin for the studied Eocene potassic magmatism. These results demonstrate that the inheritance a soft and buoyant precollisional Tibetan lithosphere may have conditioned the growth and the present-day structure of the Tibet Plateau.

Plain Language Summary The Tibetan Plateau is the largest relief on the Earth's surface, but also one of the least understood geodynamic phenomena, due to the lack of constrain on its growth evolution and mechanism. Here we have discovered, enclosed in Eocene (35-Ma-old) lavas from Central Tibet, hydrous and carbonated minerals derived from the underlying upper mantle, which reveal an unsuspected abundance of water and CO₂ in this upper mantle. We show that, consequently, the upper mantle beneath Central Tibet has been anomalously weak since before the collision of India with Asia. It was previously thought to have disappeared, foundered in a process called “delamination,” but we demonstrate here that this was an artifact: Most of the tibetan mantle is still there, but it is very weak and therefore does not appear on the seismic images. This implies that models expecting the Tibet Plateau to be a result of a delamination process are probably wrong; instead, we propose a model in which the weak upper mantle beneath our study area was easily indented by the strong adjacent continental block; this model manages to explain both Eocene magmatism and uplift in our study area.

1. Introduction

Magmatism has been repeatedly occurring on the Tibetan Plateau since the onset of the India-Asia collision (ca. 45–65 Ma), but melting processes in such postcollisional context are still debated. Petrogenetic models for the Tibetan postcollisional magmatic rocks usually fall into two families: subduction-induced melting (including, or not, slab retreat and slab break-off processes) or melting related to lithospheric thinning and

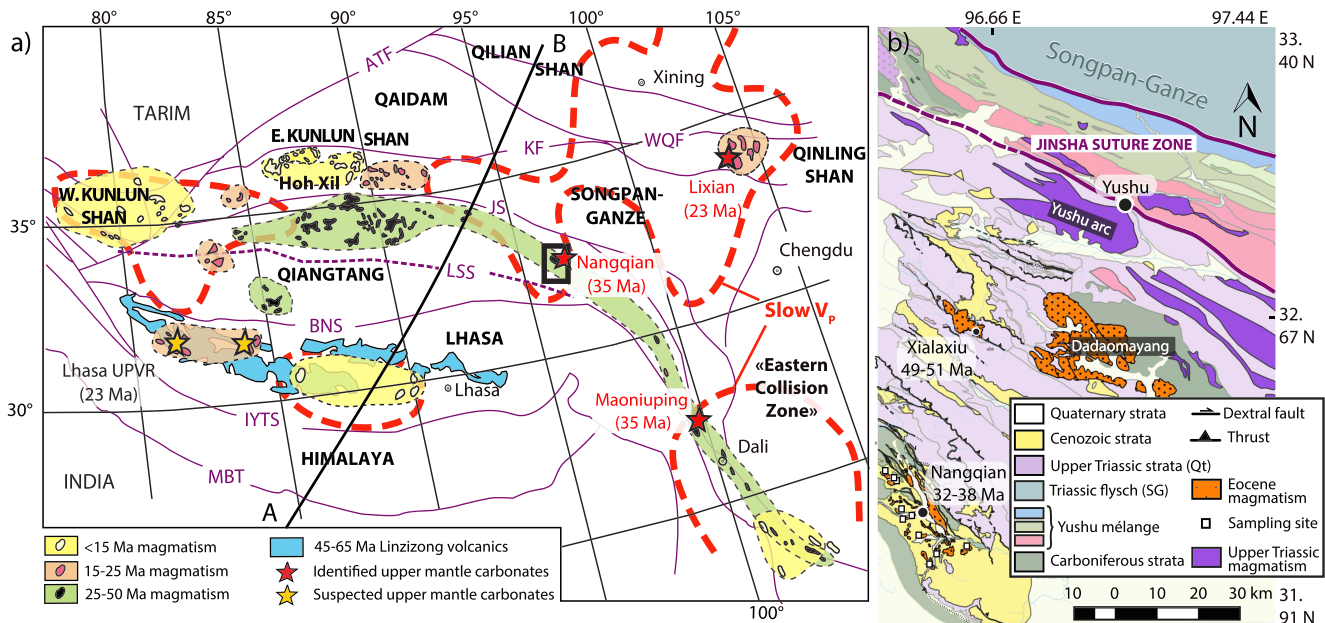


Figure 1. (a) Map of the Tibetan Plateau showing the distribution of Cenozoic magmatism, adapted from Liu et al. (2015), Mo et al. (2006), and Yang and Woolley (2006). Major sutures and structural boundaries are indicated by purple and blue lines. The thick red dotted lines delimitate areas of slow V_p perturbation in the Tibetan upper mantle, based on the tomographic horizontal slice at 150 km of Wang et al. (2019). Stars indicate where mantle metasomatism by C-rich agents has been identified or suspected. The A-B line indicates the location of the tomographic cross section of Figure 10c. The black square indicates the location of Figure 1b. (b) Map of the studied area, with sampling locations, after Spurlin et al. (2005), Yang et al. (2012), and the Geological Survey of Qinghai Province 1:250,000 geological map (2005). Abbreviations: ATF = Altyn-Tagh Fault; BNS = Bangong Suture; IYTS = Indus-Yarlung-Tsangpo Suture; KF = Kunlun Fault; LSS = Longmu Co-Shuanghu Suture; MBT = Main Boundary Thrust; QS = Qilian Suture; WQF = Western Qinlin Fault; UPVR = Ultra-Potassic Volcanic Rocks.

asthenospheric upwelling. Melting models thus reflect the two main competing end-member models for the Cenozoic growth of the Tibetan Plateau: in the first case, stepwise localized thickening by intracontinental subductions along reactivated ancient suture zones (Meyer et al., 1998; Tapponnier et al., 2001); in the second case, continuous and homogenous thickening of the whole Tibetan lithosphere, followed by convective removal of the Tibetan lithospheric mantle (England & Houseman, 1989; Molnar et al., 1993).

Eastern Qiangtang is the region of the Tibetan Plateau where intracontinental subduction is the most substantiated (Roger et al., 2000; Wang et al., 2001): Eocene postcollisional magmatism forms there a narrow strip (< 100 km wide) parallel to the Jinsha suture (Figure 1a), is syn-contractual (Horton et al., 2002; Spurlin et al., 2005), and presents isotopic compositions compatible with the presence of subducted crustal material in the source deriving from the adjacent Songpan-Ganze terrane (Xu et al., 2016).

However, the possibility for the refractory continental lithosphere to melt during subduction is contested (Chung et al., 2005). Moreover, all tomography models reveal the presence of a low P -wave velocity anomaly in the mantle lithosphere beneath the Eastern Qiangtang and Songpan-Ganze terranes, at 100- to 150-km depth (Figure 1a; Lei & Zhao, 2016; Li et al., 2008; Replumaz et al., 2013; Wang et al., 2019). This low P -wave velocity anomaly, widely interpreted in terms of elevated temperatures, has long been supporting scenarios of convective removal or gravity-driven delamination of most of the lithospheric mantle in this area, resulting in plateau uplift by isostatic rebound (Chung et al., 2005; Jiménez-Munt & Platt, 2006; Molnar et al., 1993; Xia et al., 2011). Still, the fact that these slow seismic wave velocities may record a compositional (Zhang et al., 2014) rather than thermal anomaly in the lithospheric mantle has never been investigated thoroughly. Eventually, the geodynamics of intracontinental subduction are not straightforward and may require a peculiar rheology of the continental lithosphere (Replumaz et al., 2016).

The rheology, melting properties, and geochemical characteristics of the Eastern Qiangtang lithospheric mantle back in the earliest stages of the India-Asia collision may be appraised by the study of mantle-derived Eocene postcollisional magmatic rocks. Here, we first use a petrological approach to probe the source of 38–37 Ma mafic rocks from the Nangqian basin (Spurlin et al., 2005), which we identify as a metasomatized lithospheric mantle strongly enriched in volatiles (H_2O and CO_2). Then, we use phase equilibrium

calculation, a rheologic mixing model, and mineral flow laws to calculate the density, seismic signature, and strength of a H₂O- and CO₂-rich metasomatized peridotite mineral assemblage. Finally, we explore the geodynamical and melting behavior of such metasomatized mantle during intracontinental subduction, by the means of numerical modeling. We show that metasomatism likely resulted in a softened Eastern Tibetan lithospheric mantle in the Eocene and that this softening could have (1) facilitated the shallow continental subduction of the adjacent Songpan-Ganze terrane, (2) allowed subduction-related potassic magmatism, and (3) participated to the thickening of the Tibetan Plateau.

2. Regional Geology and Sample Description

2.1. Regional Geology

The Tibetan Plateau consists of multiple accreted continental terranes or blocks: from North to South, the Qaidam, Songpan-Ganze, Qiangtang, and Lhasa blocks (Figure 1a). Internal suture zones have been recently discovered inside the Qiangtang terrane (Li et al., 2006) and Lhasa terrane (Yang et al., 2009), dividing them into Eastern and Western Qiangtang, and Northern and Southern Lhasa. All these terranes were accreted together long before the India-Asia collision, from Paleozoic to late Mesozoic times (Yin & Harrison, 2000).

“Postcollisional” (i.e., posterior to the India-Asia collision) geological record on the Tibetan Plateau is dominated by magmatism and intramontane sedimentation. The earliest stages of this postcollisional record can be found in Central and Eastern Tibet, where a 1,500-km-long belt of Paleocene-Eocene syn-contractual volcano-sedimentary basins extends along the Jinsha suture between the Qiangtang and Songpan-Ganze terranes and continues southward in the Eastern Collision Zone (western Sichuan and Yunnan) (Figure 1a). Among them, the Nangqian basin, in Eastern Qiangtang, is located at the boundary between Central Tibet and the Eastern Collision Zone, above the southern tip of the upper-mantle *P*-wave low-velocity anomaly (Figure 1a; Wang et al., 2019). Potassic to ultrapotassic calc-alkaline rocks were emplaced there in the Eocene, from 40 to 32 Ma (Spurlin et al., 2005; Xu et al., 2016, 2019), mainly as small volume dykes and sills intruding the mudstone-dominated uppermost basin fill. Folded dykes and growth strata indicate that shortening, magmatism, and part of the sedimentation were coeval (Horton et al., 2002). In most places, intermediate, leucocratic to pinkish trachydacites occur in association with more mafic, melanocratic trachyandesites. Ignimbritic flows sometimes cap the whole volcano-sedimentary section, and plutonic stocks outcrop in four places of the basin. Older Cenozoic magmatism occurs about 50 km north of the Nangqian basin: The potassic rhyolites capping the Xialaxiu basin and the wide monzonitic granite body forming the Dadaomayang massif both show ages in the range 51–49 Ma (Roger et al., 2000; Spurlin et al., 2005). Because of their very differentiated nature (SiO₂ > 65 wt%), these rocks were not selected to study the characteristics of the local mantle source.

2.2. Sample Description

Extrusive rocks sampled in the Nangqian basin have microlithic-to-microphaneritic porphyritic textures. Trachydacites show K-feldspar, plagioclase, and amphibole phenocrysts in a matrix of feldspar + amphibole + biotite + quartz + oxides; trachyandesites show clinopyroxene, apatite, and resorbed biotite phenocrysts in a matrix of feldspar + clinopyroxene + oxides. One intrusive outcrop of porphyritic syenite was also sampled, composed of clinopyroxene and biotite phenocrysts in a matrix of feldspar + clinopyroxene + biotite + apatite + oxides.

3. Methods

3.1. Analytical Methods

3.1.1. Major- and Trace-Element Compositions

Whole-rock major and trace elements were measured at ISTerre, University Grenoble Alpes. For major elements, 50 mg of rock powder was digested in HF/HNO₃ mixture at 90°C during 5 days. Excess HF was neutralized using boric acid, and solutions were diluted with 250 ml of Milli-Q water. Major element contents were measured by Inductively Coupled Plasma-Atomic Spectrometry in Grenoble using the method given in Chauvel et al. (2011). For trace elements, 100 mg of rock powder was digested with a mixture of concentrated HF and HNO₃ at 150°C for at least 2 weeks in steel Spar bombs. Excess Hf was neutralized with HNO₃, using cycles of acid addition/evaporation. Three-hundred milligrams of a spike containing Be, Ge, In, Tm, and Bi was added to an aliquot of the rock solution corresponding to 8 mg of the initial powder. The solutions were then evaporated, diluted with 2% HNO₃ (+ 1 drop of HF), and analyzed by Inductively Coupled Plasma-Mass Spectrometry. During measurement, the signal was calibrated using the reference

material BR24 (Chauvel et al., 2011), which was run every four or five analyses. Quality of the analytical procedure was checked by analyzing blanks, international reference materials (BHVO2, BEN, and BCR2), duplicate solutions, and multiple runs of solutions. Only elements with external reproducibility < 15% are given in Table S1 in the supporting information.

3.1.2. Strontium and Neodymium Isotope Compositions

The SARM-CRPG in Nancy and SEDISOR in Brest performed the whole-rock Sr and Nd isotope analyses. Results were normalized to values of $^{143}\text{Nd}/^{144}\text{Nd} = 0.512110$ for JNd-I reference material and 0.511850 for LaJolla, and to $^{87}\text{Sr}/^{86}\text{Sr} = 0.710250$ for the reference material NIST SRM 987. Blanks were 74 pg for Nd and 137 pg for Sr. ϵ_{Nd} ratios were calculated using the CHUR isotopic composition of Bouvier et al. (2008).

3.1.3. Mineral Composition

In situ major-element compositions of mineral phases (Table S2) were obtained using the JEOL JXA-8230 Electron Microprobe at ISTerre, University Grenoble Alpes. Analytical conditions were 15-kV accelerating voltage and 12-nA beam current. The ZAF procedure was applied to reduce the raw data. The microprobe was calibrated using natural and synthetic standards. An X-ray element map of a calcite-bearing aggregate was acquired using 15-kV accelerating voltage and 10-nA beam current.

3.1.4. Carbon-Oxygen Isotope Composition of Carbonates

Stable isotope analysis of carbonates was carried out in the stable isotope laboratory of Geoscience Rennes, CNRS-University of Rennes I. Carbonates in whole-rock powders were selectively dissolved at 50°C with anhydrous phosphoric acid H₃PO₄. The released CO₂ gases were collected using a cryogenic extraction line, and their isotopic compositions were analyzed by a VG Optima triple collector mass spectrometer. Results were normalized to the values of the laboratory in-house standard Prolabo Rennes and the international standard NBS18. The analytical uncertainty is $\pm 0.2\%$ for O and $\pm 0.1\%$ for C.

3.2. Properties of a Hydrated and Carbonated Peridotite

3.2.1. Phase Equilibria Calculations

Equilibrium mineral assemblages in an H₂O-CO₂-metasomatized peridotite were calculated with the Gibbs free-energy minimization *Perple_X* program (Connolly, 2005). Pseudosections were built by using the 2002-revised version of the thermodynamic data set of Holland and Powell (1998), and an internally consistent set of solid-solution models summed up in Table S3 (Bouilhol et al., 2015; Franzolin et al., 2011; Holland & Powell, 1998; Newton et al., 1980; Powell & Holland, 1999; Wei & Powell, 2003; White et al., 2001).

Starting compositions are presented in Table S4. To model the Tibetan lithospheric mantle, we used the Average Lherzolite composition from Griffin et al. (2009), to which we added amounts of H₂O, K₂O, and CO₂ in order to simulate metasomatism: The H₂O content was fixed at 0.3 wt% (the least value to saturate the system in water), and we varied the CO₂ content in order to get the following $\frac{\text{CO}_2}{\text{CO}_2+\text{H}_2\text{O}}$ molar ratios: 0; 0.3; 0.8; 0.96. The Primitive Upper Mantle composition of McDonough and Rudnick (1999) was used to model the asthenosphere.

3.2.2. Extraction of Mineral Assemblage Properties Along Geotherms

In order to compare thermal and compositional effects on the geophysical signature of the lithosphere, we extracted from the calculated pseudosections seismic velocity and density profiles along two end-member geotherms. The geotherms were built assuming pure stationary conduction between two thermal boundaries, the crust-mantle Mohorovici discontinuity (Moho) and the lithosphere-asthenosphere boundary (LAB). The Moho depth was fixed at 70 km (e.g., the present-day Moho depth beneath Eastern Qiangtang), while the LAB temperature was set at 1,340°; end-member geotherms were defined by changing the Moho temperature and LAB depth:

- for the “cold” geotherm (CG), the Moho temperature was fixed at 700° and the LAB depth at 200 km. It reflects the thermal structure of cratonic areas such as India and the North China craton.
- for the “hot” geotherm (HG), the Moho temperature was fixed at 1,100° and the LAB depth at 130 km, as would be expected from a thinned lithospheric beneath Central Tibet.

The internal *Perple_X* approach was chosen for density and seismic velocity calculation (Connolly & Kerrick, 2002), which uses shear moduli coefficients from Bina and Helffrich (1992).

3.2.3. Aggregate Viscosity Calculations

Laboratory experiments suggest that for steady-state flow deformation of minerals and rocks, the strain rate $\dot{\epsilon}$ and stress σ fit a power law relation of the form

$$\dot{\epsilon} = A\sigma^n \exp\left(-\frac{Q}{RT}\right), \quad (1)$$

where A , n , Q , R , and T are the preexponential factor, stress exponent, activation energy, gas constant, and absolute temperature, respectively (Kohlstedt et al., 1995). The corresponding viscosity is given by

$$\eta = \frac{\sigma}{2\dot{\epsilon}} \quad (2)$$

In order to assess the rheology of a H₂O- and CO₂-metasomatized peridotite, we used the Minimized Power Geometric mixing model of Huet et al. (2014) to calculate the bulk flow law parameters (\bar{n} , \bar{A} , \bar{Q}) of the equilibrium mineral assemblages modeled with Perple_X from the flow law parameters of their constitutive minerals:

$$\bar{n} = \frac{\sum_i \phi_i a_i n_i}{\sum_i \phi_i a_i} \quad (3)$$

$$\bar{Q} = \frac{\sum_i \phi_i a_i Q_i}{\sum_i \phi_i a_i} \quad (4)$$

$$\bar{A} = \prod_i A_i^{\phi_i a_i / \sum_j \phi_j a_j} \times \left(\sum_i \frac{\phi_i n_i}{n_i + 1} \right)^{-\bar{n}} \prod_i \left(\frac{n_i}{n_i + 1} \right)^{\phi_i a_i n_i / \sum_j \phi_j a_j}, \quad (5)$$

where n_i , Q_i , and A_i are the flow law parameters of phase i , ϕ_i its volume fraction in the aggregate, and the parameter a is defined for each phase as $a_i = \prod_{j \neq i} (n_j + 1)$. This method assumes that the rock can be considered homogeneous and isotropic and that all phases deform by a single mechanism, here by dislocation creep.

We used the mineral proportions given by the pseudosections along both end-member geotherms (Table S6a). Published flow law parameters used for each mineral phase (Bystricky & Mackwell, 2001; Bystricky et al., 2016; Holyoke et al., 2014; Kawazoe et al., 2009; Kronenberg & Pinkston, 1990; Li et al., 2006; Ohuchi et al., 2011) are given in Table S5. The strain rate was fixed at $\dot{\epsilon} = 10^{-14} \text{ s}^{-1}$. Resulting bulk flow law parameters for each modeled peridotite composition are listed in Table S6b.

4. Results

4.1. Whole-Rock Chemistry

Fourteen samples of mafic to intermediate lavas and two samples of syenite were selected for mineral and whole-rock geochemical analysis. The data are reported in Figure 2 and given in Table S1.

Intermediate and mafic lavas are potassic to highly potassic ($\text{SiO}_2 = 47\text{--}63 \text{ wt}\%$; $\text{K}_2\text{O}/\text{Na}_2\text{O} = 0.8\text{--}2.2$) and the syenite is ultrapotassic ($\text{K}_2\text{O}/\text{Na}_2\text{O} = 3.4\text{--}4.9$). Samples have high rare earth element contents ($\text{La}_N = 84\text{--}315$, where N is the normalization to mantle values of McDonough & Sun, 1995), with fractionation of heavy rare earth element ($\text{Gd}/\text{Yb}_N > 3$), and a typical arc signature with depletion in high field strength elements ($\text{Nb}/\text{Th}_N = 0.06\text{--}0.32$; Figure 2b). In the $\epsilon_{\text{Nd}}(t)$ versus $^{87}\text{Sr}/^{86}\text{Sr}(t)$ diagram (Figure 2c; $t = 35 \text{ Ma}$), our samples define a trend of decreasing $\epsilon_{\text{Nd}}(t)$ (from -0.8 to 1.1) with increasing $^{87}\text{Sr}/^{86}\text{Sr}(t)$ (from 0.7049 to 0.7055). Similar isotopic compositions have been reported by Sun et al. (2001), Spurlin et al. (2005), and Xu et al. (2016) for other lavas and intrusive rocks from the Nangqian basin.

4.2. Xenocrysts and Xenoliths in Nangqian Magmatic Rocks

Two distinct populations of xenocrysts and micro-xenoliths, hosted in two different rock types, were identified in our samples.

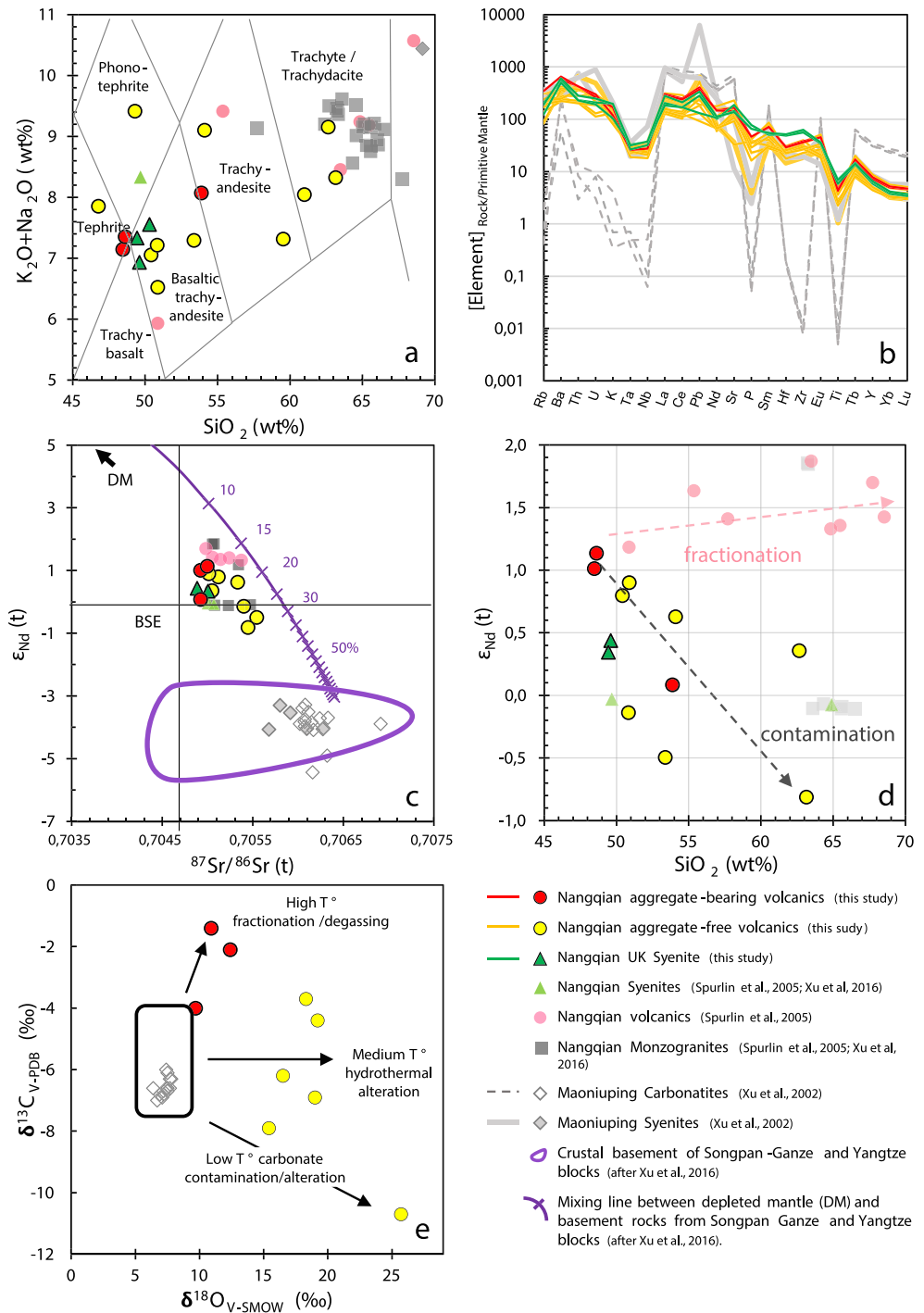


Figure 2. (a–d) Major-element, trace-element, and isotopic composition of studied samples, compared with literature data from Nangqian and from the Eastern Collision Zone syeno-carbonatitic complex of Maoniuping (Western Yunnan). (a) Total Alkali Silica diagram. Classification fields after Le Maitre et al. (2002). (b) Incompatible trace element concentrations normalized to primitive mantle values of McDonough and Sun (1995). (c) $\epsilon_{Nd}(t)$ versus $^{87}Sr/^{86}Sr(t)$ ($t = 35$ Ma). As shown by Xu et al. (2016), Nangqian Sr-Nd isotopic ratios are compatible with a depleted mantle source (DM) mixed with 15–25% of subducted Songpan-Ganze crustal rocks. (d) $\epsilon_{Nd}(t)$ versus SiO_2 content ($t = 35$ Ma). Note the crustal contamination trend in our sample suite, compared with the homogeneous $\epsilon_{Nd}(t)$ measured by Spurlin et al. (2005). (e) Carbon and oxygen stable isotope composition of carbonates. The “carbonatite box” refers to the expected values for mantle-derived carbonatite (Taylor et al., 1967). The arrows show the different processes leading to variations from these primary values (Deines, 1989).

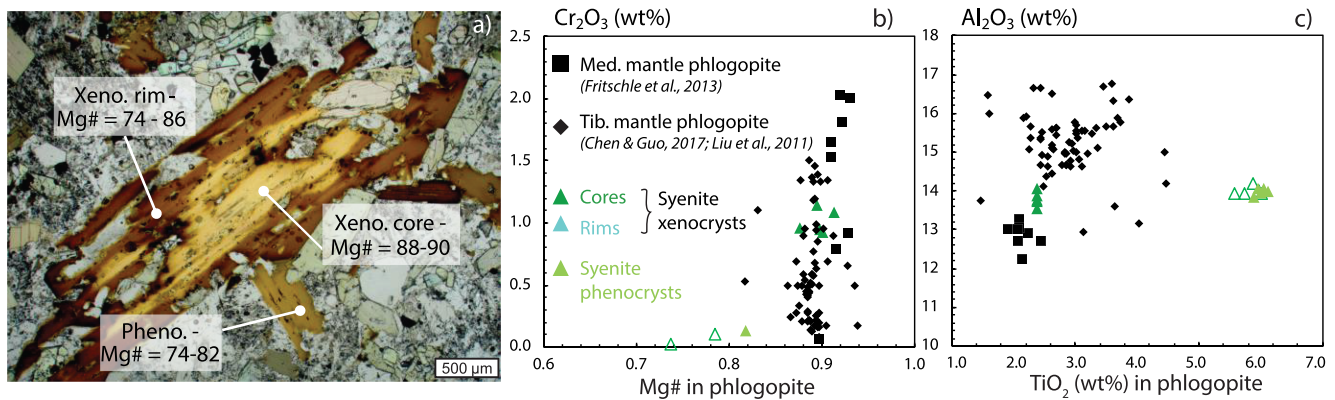


Figure 3. Phlogopite within the ultrapotassic syenite. (a) Photomicrograph of mantle xenocrysts (Xeno.) and host-rock phenocrysts (Pheno.). (b and c) Two-oxide diagrams for the two families of phlogopite crystals (mantle xenocrysts and host-rock phenocrysts) within the ultrapotassic mafic syenite. Data for Mediterranean and Tibetan mantle phlogopites were included for comparison, from Fritschle et al. (2013), Cheng and Guo (2017), Liu et al. (2011).

4.2.1. Phlogopite Xenocrysts in Ultrapotassic Syenites

The samples of ultrapotassic syenite contain large zoned phlogopite grains with reddish resorbed cores (Figure 3a). These cores have high MgO (Mg# = 88–90) and Cr₂O₃ contents (Cr₂O₃ = 0.9–1.8 wt%) and low TiO₂ contents (TiO₂ = 2.37–2.38 wt%), compared to the rims and to small groundmass phlogopite (Figures 3b and 3c; Table S2). These core compositions are intermediate between Tibetan mantle phlogopites (Cheng & Guo, 2017; Liu et al., 2011) and Mediterranean mantle phlogopites (Fritschle et al., 2013; Figure 3). Based on their resorbed shape and on their composition, we interpret the cores of the large phlogopite grains as mantle xenocrysts.

4.2.2. Cognate Clinopyroxene Micro-Xenoliths in Mafic Potassic Lavas

Three samples of mafic potassic lavas (SiO₂ = 48–54 wt%, Mg# = 59–61) contain aggregates (10 to 15 vol%) with coarse-grained cumulate textures and consisting of finely zoned clinopyroxene (diopside, En_{36–49}Wo_{45–49}) crystals, rare resorbed magnesian phlogopite (Mg# = 80–85), and calcite that fills the grain boundaries and cracks, often in association with apatite, ilmenite, K-feldspar, and rarely barite (Figure 4a).

The cores of the clinopyroxene grains (Mg# = 90) in the aggregates crystallized from mantle-derived liquids (Mg# ~ 70, calculated using the $K_D^{Fe-Mg}_{Cpx-liq}$ value of 0.27 from Irving & Frey, 1984), more mafic than the host lava (Mg# ~ 60; Figures 4c and 4d; Table S2). This shows that these clinopyroxene aggregates are microxenoliths of an ultramafic rock (a clinopyroxenite), likely of cumulative origin, and cognate with the host lavas.

The sharp contacts between calcite and the host lava at the edges of the cognate microxenoliths (Figure 4b) suggest that the carbonates crystallized before the incorporation of the microxenoliths into the host lavas. In the three samples described here, this microxenolith-bounded calcite is the only carbonate observed, and it differs texturally from secondary carbonates that fill vacuoles or partially replace clinopyroxene grains in other lava samples. Its carbon and oxygen isotope ratios ($\delta^{13}C = -4\text{‰}$ to -2‰ ; $\delta^{18}O = 10\text{‰}$ to 13‰ ; Figure 2e) extend from the primary igneous carbonatite values (Taylor et al., 1967) along a high-temperature fractionation-degassing trend (Deines, 1989). These isotopic compositions are distinct from the high- $\delta^{18}O$ (17‰ to 26‰) and low- $\delta^{13}C$ (-9 to -11‰) values of the secondary carbonates present in other samples, typical of medium- to low-temperature conditions of precipitation. These results indicate that calcite in the cognate microxenoliths is part of the cumulate magmatic assemblage, as a late magmatic phase.

4.3. Density, Seismic Signature, and Strength of a Hydrated and Carbonated Peridotite

4.3.1. P-T Pseudosections

P-T pseudosections of dry and metasomatized peridotites calculated with *Perple_X* are given in Figure 5. The addition of H₂O and K₂O to the starting Average Lherzolite composition (model M1_0, Figure 5c) leads to the stabilization of phlogopite, and amphibole at low pressures and temperatures; it also reduces the solidus by 320°C (at 1 GPa); by comparison, the experimental solidus of Falloon and Green (1990) (yellow line) is even 80–100°C lower.

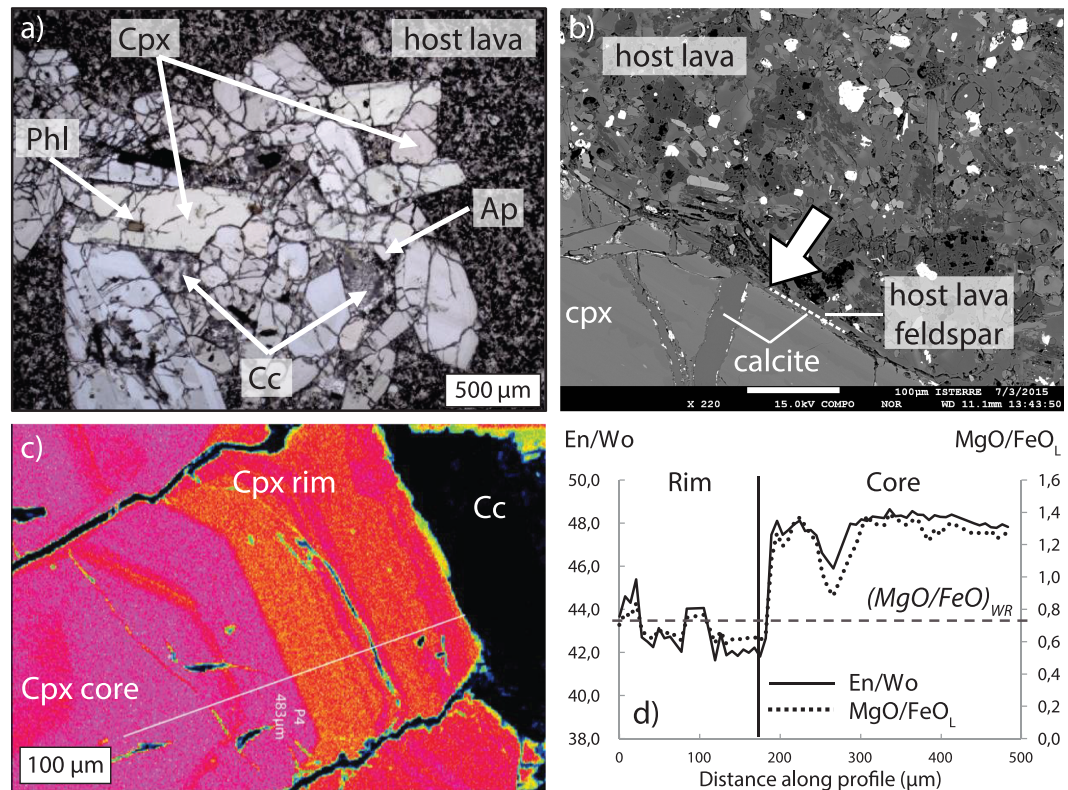


Figure 4. Calcite-bearing clinopyroxene aggregate within a potassic tephrite (sample YU-14-35). (a) Photomicrograph. (b) EBSD close-up view on the contact between the aggregate and its host lava. (c) Magnesium element map of an aggregate clinopyroxene. The location of “P4” profile of Figure 4d is indicated. (d) Composition of the clinopyroxene along the P4 profile in Figure 4c. For comparison, MgO/FeO_{WR} ratio of the whole-rock (lava + aggregates) and MgO/FeO_L ratio of the liquid in equilibrium with clinopyroxene ($K_D^{Fe-Mg}_{Cpx-liq} = 0.27$; Irving & Frey, 1984) are indicated. Ap = apatite; Cc = calcite; Cpx = clinopyroxene; Phl = phlogopite; En = enstatite content; Wo = wollastonite content.

Further addition of CO_2 to the system leads to the stabilization of a magnesian carbonate, which is replaced by free CO_2 at low pressures/high temperatures and/or by carbonate melt at high temperatures (Figure 5d). Appearance of the carbonate melt occurs at temperatures decreasing from $1,500^\circ C$ at 1.5 GPa to $1,180^\circ C$ at 2.5 GPa, drawing a solidus with a pronounced ledge, whereas the silicate solidus is not significantly modified by the addition of CO_2 . The shapes of the carbonate and silicate solidi are consistent with experiments (green lines, see the review by Hammouda & Keshav, 2015), but they are strongly shifted toward higher temperatures. Our models thus unaccurately represent the melting behavior of a carbonated peridotite and will only tackle the solid aggregate properties.

The mineral compositions of the different models have little evolution along the geotherms (mineral modes are reported in Table S5). In the metasomatized lherzolite models, the phlogopite abundance (5 vol%) reflects the fixed K_2O content imposed to the system (0.5 wt%); its formation results in a small decrease in olivine, orthopyroxene, and garnet abundances. Carbonate (from 0 to 10 vol% depending on the initial CO_2 content) forms at the expense of olivine (which amount decreases from 61 to 43 vol%) and is accompanied with an increase in orthopyroxene abundance (from 13 to 23 vol%).

4.3.2. Density and Seismic Velocity Profiles

Density and seismic velocity profiles realized along the two geotherms allow to compare the effects of compositional versus thermal variations on these geophysical observables. Our reference model is the Average Lherzolite composition under the cold geotherm (M1_dry-CG). As can be seen in Figure 6, adding H_2O , K_2O , and CO_2 to the Average Lherzolite composition while keeping the cold geotherm (Models M1_0 to M1_096) has nearly the same consequences on densities and seismic velocities than using the hot geotherm on the starting dry, unmetasomatized Average Lherzolite composition (Model M1_dry-HG): At 4.5 GPa,

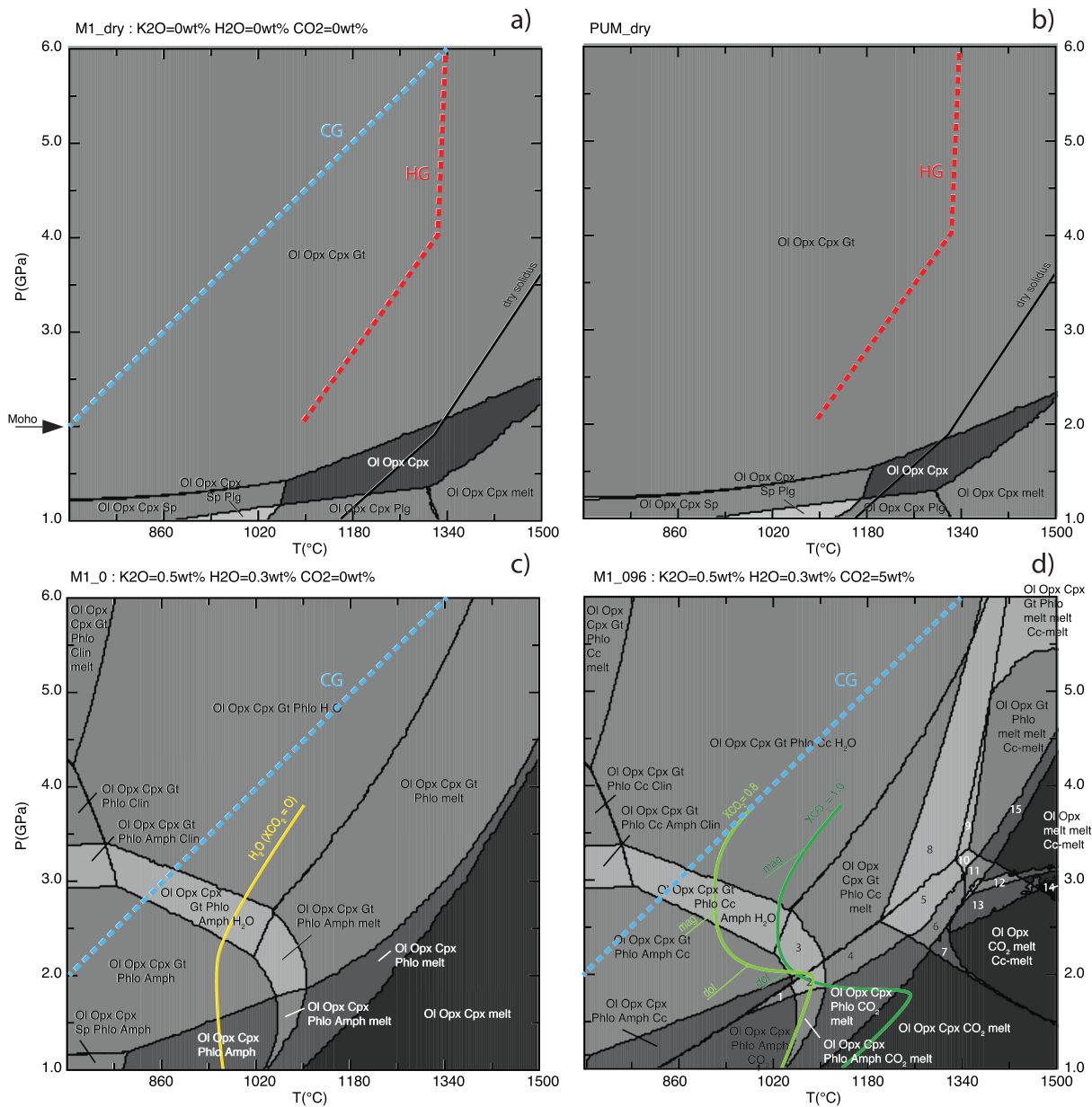


Figure 5. Modeled pseudosections, in the CO_2 -NCKFMASH system. The blue and green dashed lines are the “cold” (CG) and “hot” geotherms (HG) used for density and seismic wave velocity modeling. Solid lines are experimental solidi of Falloon and Green (1990) for dry, hydrated, and carbonated Hawaiian pyrolites (molar XCO_2 is reported). Mineral abbreviations: Amph = amphibole; Cc = carbonate; Cc-melt = carbonate melt; Clin = clinzoizite; Gt = garnet; melt = silicate melt; Ol = olivine; Opx = orthopyroxene; Phlo = phlogopite; Plg = plagioclase. Labeled fields in (d) are (1) Ol Opx Cpx Gt Phlo Amph CO_2 , (2) Ol Opx Cpx Gt Phlo Amph CO_2 melt, (3) Ol Opx Cpx Gt Phlo Amph Cc melt, (4) Ol Opx Cpx Gt Phlo CO_2 melt, (5) Ol Opx Cpx Gt Phlo melt C-melt CO_2 , (6) Ol Opx Cpx Phlo melt Cc-melt CO_2 , (7) Ol Opx Cpx CO_2 melt Cc-melt, (8) Ol Opx Cpx Gt Phlo Cc melt Cc-melt, (9) Ol Opx Gt Phlo Cc melt melt Cc-melt, (10) Ol Opx Gt Phlo melt melt Cc-melt CO_2 , (11) Ol Opx Phlo melt melt Cc-melt CO_2 , (12) Ol Opx melt melt melt Cc-melt CO_2 , (13) Ol Opx melt melt Cc-melt CO_2 , (14) Ol Opx melt Cc-melt, and (15) Ol Opx Phlo melt melt Cc-melt.

the densities of the modeled lherzolites are reduced from 3,379 to 3,323–3,354 kg/m^3 , and seismic waves are slowed, from 8.14 to 7.96–7.99 km/s for P -waves and from 4.56 to 4.42–4.46 km/s for S -waves.

4.3.3. Viscosity Profiles

The viscosity profiles calculated for each mineral composition of the lherzolite models along the cold and/or hot geotherms are presented in Figure 7. Temperature exerts here the strongest control on the bulk strength of the mineral aggregate: For the dry Average Lherzolite composition (M1_ dry), the viscosity at 70 km is lowered from 3.16×10^{22} to 1.26×10^{20} Pa s when using the hot geotherm. The effects of metasomatism (Models M1_ 0 to M1_ 096) on bulk viscosity, studied here under the cold geotherm conditions, are not

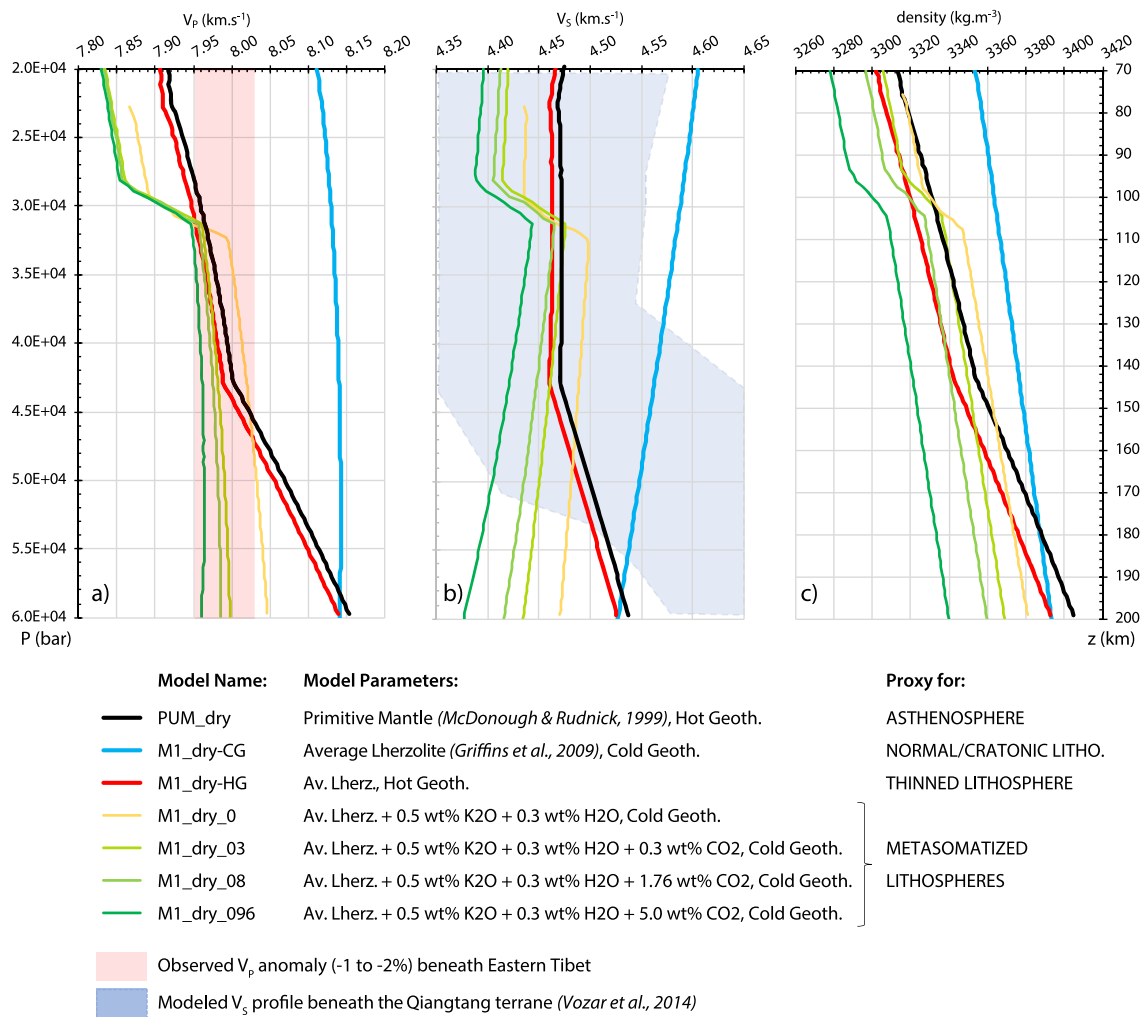


Figure 6. Results of calculation of (a) P -wave velocities, (b) S -wave velocities, and (c) densities along an 70- to 200-km depth profile for different mantle lithologies (dry or metasomatized) and thermal conditions (cold or hot). HG = hot geotherm; CG = cold geotherm.

straightforward: carbonates have a very low strength (Holyoke et al., 2014), but since their formation is coeval with that of orthopyroxene, the resulting bulk strength of the metasomatic mineral assemblage is also strongly dependent on the flow law chosen for orthopyroxene: While using the parameters of Ohuchi et al. (2011) results in a significant metasomatic weakening of the lherzolite (from 5.75×10^{21} to 1.32×10^{21} Pa.s at 70-km depth), using the parameters of Bystricky et al. (2016) results in a higher strength for the reference dry lherzolite and very limited metasomatic softening (< 2 Pa.s; Figure 7a).

Moreover, if we consider not only the formation of hydrated and carbonated minerals but also the hydration of nominally anhydrous minerals (olivine and clinopyroxene) through the use of “wet” flow laws (Dimanov & Dresen, 2005 and Karato & Jung, 2003, respectively), the maximum deviatoric stress of the metasomatic aggregates may become nearly one order of magnitude smaller than the dry one (8.32×10^{20} Pa.s at 70 km; Figure 7b).

5. Discussion

5.1. A Carbonate- and Phlogopite-Bearing Tibetan Mantle

The highly to ultrapotassic composition of the studied mafic and intermediate samples and their arc-like trace-element signature (i.e., negative anomaly in Nb-Ta) point toward a lithospheric mantle source metasomatized by hydrous fluids. The occurrence of mantle phlogopite xenocrysts in the ultrapotassic syenite provides further evidence for the hydrous metasomatism of the mantle source already identified from

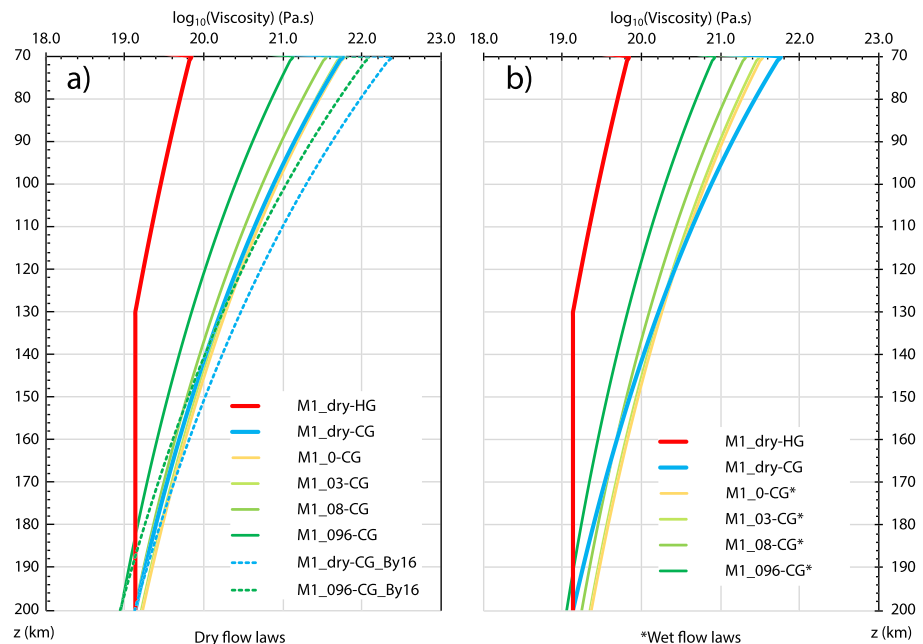


Figure 7. Viscosity profiles for the different lherzolite models, calculated from the mineral proportions determined with *Perple_X*. In (a), solid lines were built using the orthopyroxene flow parameters of Ohuchi et al. (2011), whereas the two dashed lines were built using the orthopyroxene flow parameters from Bystricky et al. (2016). In (b), “wet” flow laws have been used for olivine (Karato & Jung, 2003) and clinopyroxene (Dimanov & Dresen, 2005) in the metasomatized models (starred names).

whole-rock chemical data. Melting of a phlogopite-bearing peridotite produces a range of mafic to intermediate potassic melts (Condamine & Médard, 2014) similar to those observed in Nangqian. Other occurrences of Cenozoic (ultra)potassic lavas in Tibet (Ding et al., 2007; Guo, 2006; Jiang et al., 2006; Sun et al., 2001; Williams, 2004; Xu et al., 2016) could be viewed as so many surface expressions of phlogopite-bearing domains within the Tibetan mantle.

In parallel, the calcite-bearing cognate microxenoliths occur in mafic lavas with Sr-Nd isotope compositions ($\epsilon_{\text{Nd}}(t) = 0$ to 1 and $^{87}\text{Sr}/^{86}\text{Sr}(t) \sim 0.7050$) that do not point toward a significant interaction with crustal material. Rather, the trend of Nd isotope ratios versus SiO_2 suggests that two of the microxenoliths-bearing lavas represent the mafic end-member from which the other xenolith-free lavas evolved, either by fractional crystallization (volcanics analyzed by Spurlin et al., 2005; Figure 2d) or by crustal contamination (this data set and syenites analyzed by Spurlin et al., 2005; Figure 2d). The formation of magmatic calcite in the cognate microxenoliths therefore requires that the mantle-derived melts from which they crystallized were initially rich in CO_2 . The stable isotope composition of this magmatic calcite, which plots along the mantle carbonatite fractionation trend in Figure 2e, shows that this feature was inherited from the mantle source. The metasomatism of the mantle lithosphere below Nangqian also involved, therefore, a CO_2 -rich agent. We thus argue that the metasomatized lithospheric mantle source below Nangqian in Eocene times was a phlogopite-bearing carbonated peridotite.

5.2. A Paleo-Tethyan Inheritance in the Lithospheric Mantle of Eastern Tibet

The calcite-bearing cumulate xenoliths identified in some Eocene mafic lavas from the Nangqian basin are the most direct evidence so far for the presence of CO_2 in the Tibetan lithospheric mantle. Nevertheless, Cenozoic carbonatites with mantle carbon and oxygen isotope ratios (Figure 2e; Hou et al., 2006) have been identified in two areas immediately adjacent to the Tibetan Plateau: the Maoniuping area in the Eastern Collision Zone and the Lixian area in the Western Qinlin Range (Figure 1a; Yang & Woolley, 2006; Hou et al., 2006; Yu et al., 2003; Lai et al., 2014). In both places, carbonatitic rocks were emplaced in association with (ultra)potassic rocks (lamprophyres and kamafugites, respectively), in transpressional settings. This suggests that the strong enrichment in volatiles (H_2O and CO_2) of the lithospheric mantle was not specific to the Nangqian area but may also have concerned other mantle domains beneath Eastern Tibet during the Cenozoic.

The source of carbon in the lithosphere may have been either subducted carbonates or CO₂-bearing melts from the asthenosphere (Huang et al., 2010). The carbonatites of Maoniuping and Lixian, as well as the carbonate-bearing cognate microxenoliths of Nangqian lavas, occur close (< 100 km) to two major Mesozoic suture zones: the Kunlun-Qinlin-Dabie and Jinsha sutures (Figure 1a). These sutures resulted from the closure of the Paleo-Tethys, first beneath the North China Craton at circa 230 Ma, then beneath the Qiangtang terrane at circa 200 Ma (Figure 10a; Roger et al., 2010). This localization, combined with the typical arc signature of Nangqian and Maoniuping (ultra)potassic rocks (Figure 2b), suggests that the influx of carbon into the Eastern Tibetan lithospheric mantle resulted from the subductions associated with the Mesozoic accretion of continental blocks to the southern margin of Eurasia. In the Maoniuping area, Xu et al. (2019) recently proposed that lithospheric mantle metasomatism could relate to even older, Neo-Proterozoic accretion processes.

Although oceanic slab-fluxing processes can easily account for the hydration of the mantle wedge and the formation of mantle phlogopite (Wyllie & Sekine, 1982), subduction of a significant amount of carbonated lithologies would be required to generate a carbonated peridotite. Platform carbonates are abundant in the Paleozoic basement sequences of Eastern Qiangtang (Hou et al., 2003). The Songpan-Ganze block is covered by a rather carbonate-poor Triassic flysch sequence (She et al., 2006), and the nature of its basement is unknown, but in its easternmost part, the flysch sequence lies on a Neoproterozoic carbonated passive-margin sequence common to the Songpan-Ganze and South China blocks (Wu et al., 2016). Moreover, the Jinsha suture zone, immediately northeast of the studied area, exposes various Carboniferous to Permian carbonated lithologies: limestone, carbonaceous schists and cherts, and calcareous sandstone (Wang et al., 2000). Thus, carbonate-rich sediments were certainly present at the margins of the colliding Qiangtang and Songpan-Ganze blocks in the Mesozoic, and their subduction during the late stages of the Paleo-Tethys closure is a plausible source for mantle carbonatation. Involvement of some continental margin in these Mesozoic subductions has indeed been proposed to explain the genesis of Late Triassic granitoids from Eastern Qiangtang, by melting of subducting Songpan-Ganze flysch (Lu et al., 2017). It is also consistent with the Sr-Nd isotope ratios of the most felsic Eocene Nangqian rocks, which point toward a source metasomatism by crustal fluids or melts derived from the Songpan-Ganze basement (Figure 2c; Xu et al., 2016).

We thus propose that Mesozoic closure of the Paleo-Tethys, and subsequent continental subductions, resulted in the formation of hydrated and carbonated mantle wedges within the Eastern Tibetan lithosphere (Figures 10a and 10b). Considering the apparent tectono-magmatic quiescence observed in Eastern Tibet during most of the Middle and Late Cretaceous (Airaghi, 2017; Clark et al., 2010), under the oxidizing conditions of the upper mantle (Mattioli et al., 1989), and in the normal to cold thermal environment generated by the oceanic subductions, the subducted carbonates likely remained stable in the lithospheric mantle until the Cenozoic, when they were remobilized by magmatism associated with the far-field effects of the India-Asia collision.

5.3. Geodynamical Consequences of a Hydrated and Carbonated Mantle Beneath Eastern-Central Tibet

5.3.1. A Soft and Buoyant Lithospheric Mantle

Our modeling results show that a H₂O- and CO₂-rich metasomatized lithospheric mantle would have been much less dense than a pristine one and buoyant over the asthenosphere (Figure 6c): This precludes any process of gravity-driven delamination of the metasomatized lithosphere root of the Qiangtang terrane. On the other hand, analog modeling has shown that subduction of a buoyant continental lithosphere is possible in a collisional context similar to the India-Asia collision (“collisional subduction”; Pitard et al., 2018; Replumaz et al., 2016).

Rheological calculations suggest that this density decrease would come along with a significant strength drop (Figure 7), due to the low strength of the metasomatic minerals formed (carbonate and phlogopite). Nevertheless, a quantitative estimate of this strength drop is difficult, primarily because of the limited data about the rheology of mantle minerals. Apart from olivine, which has been the focus of numerous works, the available flow laws for pyroxenes, garnet, and phlogopite are still limited in number and disparate in quality (Karato, 2010). We have underlined here the discrepancies concerning the behavior of orthopyroxene at lithospheric mantle conditions (Figure 7a), but the flow laws of garnet may also be problematic as they could

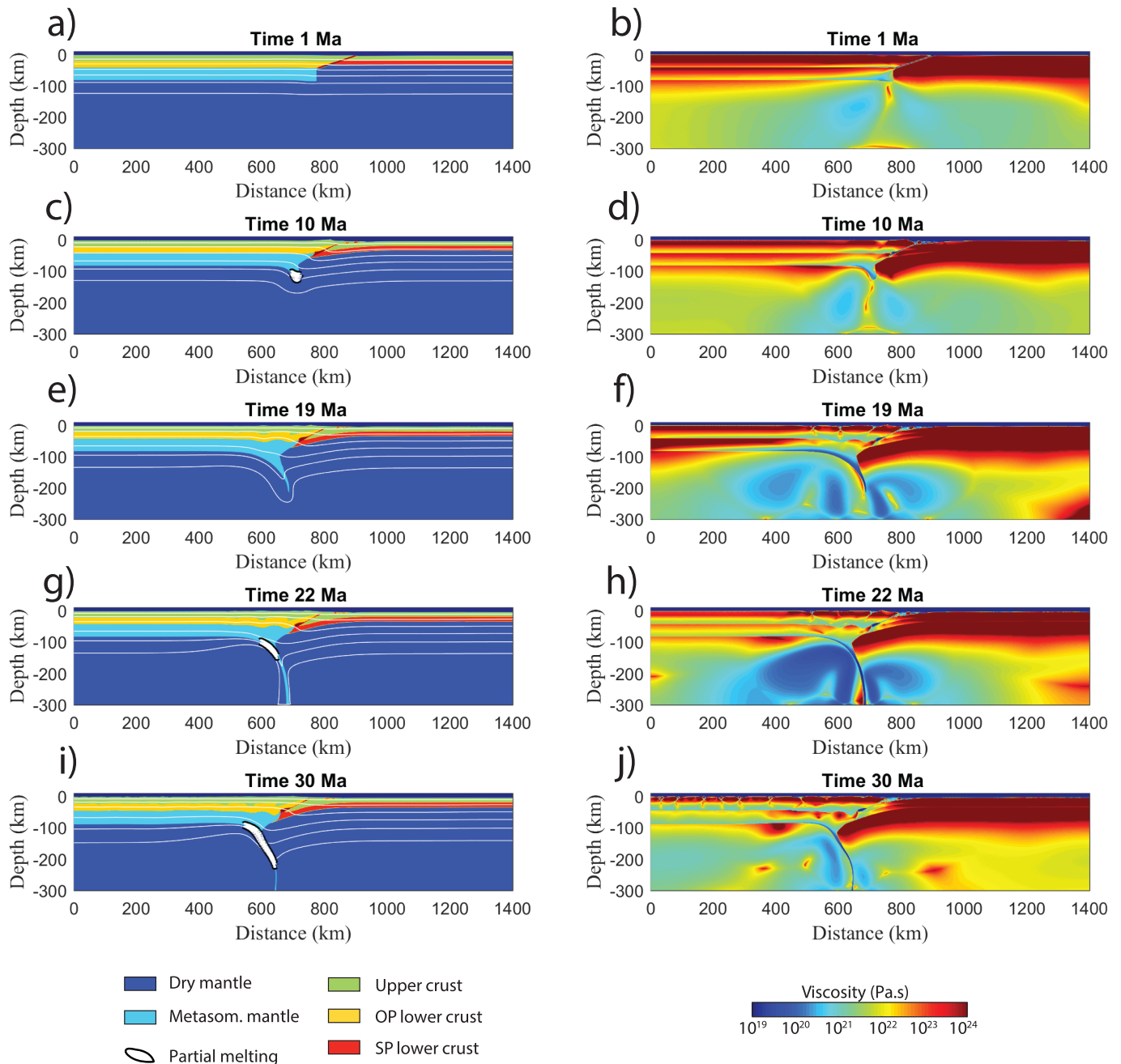


Figure 8. Time evolution of the rectangle-shaped reference model. Left panel, material fields overlaid with isotherms, and location of partial melting in the metasomatized mantle. Right panel, viscosity field. OP = overriding plate; SP = subducting plate.

underestimate garnet strength (Shinevar et al., 2015). Moreover, rheological data for these two minerals under “wet” conditions are lacking.

To describe the rheology of orthopyroxene, we favor here the flow law parameters of Ohuchi et al. (2011) since they were experimentally determined at pressure and temperatures (1.3 GPa and 973–1373 K) relevant for the lithospheric conditions studied here, while those of Bystricky et al. (2016) are extrapolated from 300–450 MPa. With these parameters, our mixing models predict that the viscosity of the metasomatized mantle could be 1 order of magnitude smaller than that of a dry one (Figure 7a).

We did not include in our calculations the effects the water fugacity (f_{H_2O}), which can be expressed as a pre-exponential term in equation (1) and thus tend to decrease the viscosity. Since for pressures above

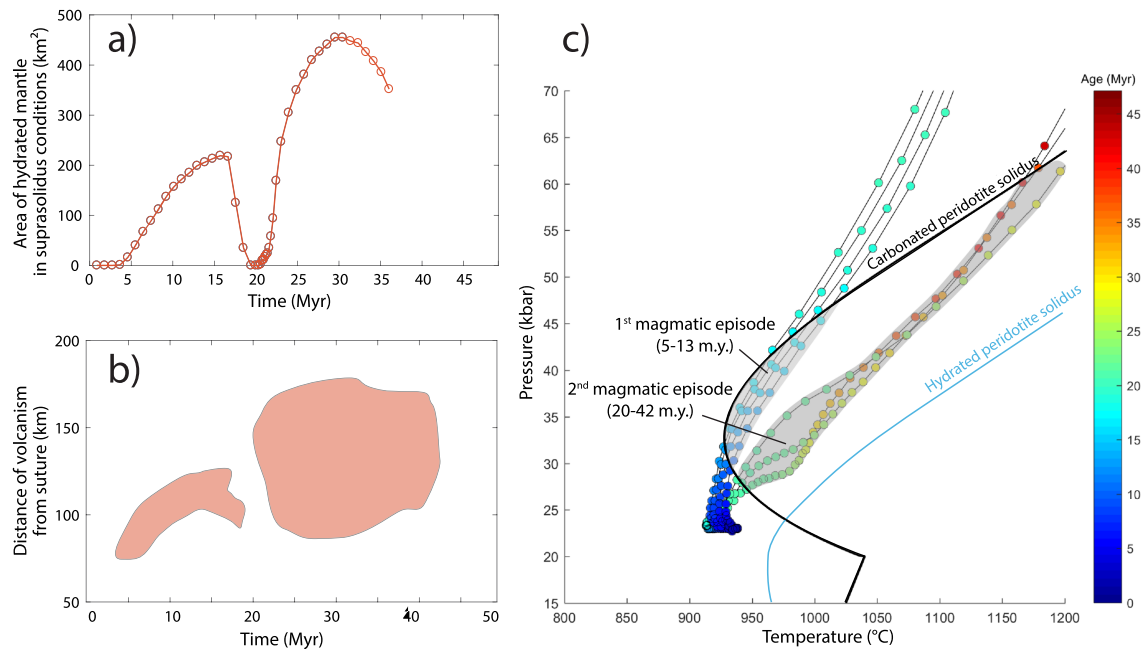


Figure 9. Characteristics of the magmatism in the rectangle-shaped reference model. (a) Area of the metasomatized mantle in suprasolidus conditions as a function of time. (b) Distance between inferred volcanism at the surface (vertical to the partial melting area at depth) and the suture zone, as a function of time. (c) P - T path of representative particles in the downwelling metasomatized mantle. The solidi of hydrated and carbonated peridotites are from Wallace and Green (1988).

0.5 GPa, f_{H_2O} increases exponentially with $\frac{P}{RT}$ (Karato, 2010), a more accurate estimate of the viscosities of metasomatized mantle models (M1_0 to M1_096) could be lowered by 10^1 to 10^2 Pa.s.

In the following, we discuss the geodynamic consequences of such a soft and buoyant lithospheric mantle on the behavior of an intracontinental subduction zone, in order to determine whether a Cenozoic subduction of the Songpan-Ganze terrane beneath the metasomatized Eastern Qiangtang terrane along the Jinsha suture would have been able to explain Eocene magmatism and crustal thickening in our study area.

5.3.2. A Specific Melting Process in Intracontinental Subduction Context

We performed thermomechanical modeling of such intracontinental subduction, using Underworld (Moresi et al., 2007) to solve the equations of momentum, continuity, and energy and to track material properties. Mathematical formulations of this code (Cramer et al., 2012; Moresi et al., 2007; Turcotte & Schubert, 2014) and detailed modeling parameters are given in the supporting information. The solidus of carbonated peridotite of Wallace and Green (1988) was used to postprocess the partial melting regions of the metasomatized mantle during subduction.

5.3.2.1. Modeling Results

In the reference model (R2*), the Eastern Qiangtang metasomatized mantle has a rectangle shape, a density of $3,280 \text{ kg/m}^3$, and its viscosity is two times lower than that of the dry mantle forming the Songpan-Ganze lithospheric mantle and the asthenosphere, with a viscosity pre-exponential factor of $5 \times 10^5 \text{ MPa}^{-3.5} \text{ s}^{-1}$ (Tables S7 and S8; Ranalli, 1997). Modeling results for this model are presented in Figures 8 and 9.

As convergence begins, continental subduction is initiated along the crustal weak zone (Figures 8a and 8b). At 10 Ma and 70 km of convergence, this continental subduction triggers crustal thickening in the overriding plate (Figure 8d), but also downward advection of the bottom right corner of the overriding metasomatized mantle to higher pressure conditions, eventually leading to suprasolidus conditions (Figure 8c). From 19 Ma onward, crustal thickening propagates southward, forming a prowedge and a retro-wedge separated by crustal-scale shear zones (Figure 8f). Meanwhile, delayed deflection of the isotherms in the downwelling metasomatized mantle results in a return to subsolidus conditions (Figure 8c). Between 22 and 30 Ma, a progressive decoupling is observed between the subducting mantle lithosphere and the lower crust, whereas the overriding plate still undergoes continuous thickening of the upper crust, southward propagation of the

intra-crustal thrust system, and downwelling of the lower right corner of the metasomatized mantle. Uplifting of the isotherms at the basis of the downwelling corner of the metasomatized mantle triggers a second episode of partial melting (Figures 8g–8i). After 30 Ma, the reference model records a total of 210 km of convergence. This results in a quite localized thickening of the overriding crust, reaching up to 20 km in the retro-wedge to prowedge area, but only 2.5 km between 0 and 400 km along the profile, away from the suture (Figure 8i).

The overall evolution of the metasomatized mantle area undergoing suprasolidus conditions exhibits two main phases: the first one between 5 and 18 Ma affecting up to 200 km² and the second one between 22 and 30 Ma affecting up to 450 km² (Figure 9a). The *P-T* paths of representative particles inside the downwelling mantle corner show that partial melting occurs along two main downwelling thermal gradients of ~ 1.25 °C/km and ~ 2.4 °C/km, which correspond to the first and second episode of volcanism (Figure 9c). Each *P-T* path first crosses the carbonated peridotite solidus at relatively low *P-T* conditions (925–950°C and 27–32 kbar) and then crosses it back to subsolidus conditions at higher pressures (above 42 and 60 kbar). Assuming that related volcanism occurs at the surface, vertically from the suprasolidus region, it is also expected to show two stages, the first one occurring 80 to 120 km away from the suture zone and the second stage occurring in a wider range, 90 to 175 km away from the trench (Figure 9b).

Two kinds of parameters were varied to study their influence on the evolution of the model: the degree of metasomatism of the overriding lithospheric mantle and its initial shape. Varying degrees of metasomatism were studied by simultaneously varying the density and rheology of the overriding lithospheric mantle, such as when metasomatism increases, both the density and the viscosity decrease (Table S7). For the initial geometry of the metasomatized mantle, both rectangular and rectangular trapezoid shapes were tested (Figure S1).

Results are given in the supporting information (Text S3 and Figures S2 to S4). Differences from the reference model results are as follows:

- with a trapezoid initial geometry, magmatism occurs much farther from the suture zone (>150 km), and the rates of southward migration are smaller (< 2 mm/year);
- with a stronger rheology, the two magmatic episodes occur by the same rate of southward migration (~ 3 mm/year), but more than 30 Ma apart from each other;
- with a weaker rheology, magmatism stays at the same distance from the suture or even migrates northward toward the suture in case of a trapezoid initial geometry.

5.3.2.2. Melting Behavior of the Hydrated-Carbonated Lithospheric Mantle

Our geodynamical modeling results show that in presence of a soft and buoyant, H₂O- and CO₂-rich metasomatized lithospheric mantle in the overriding plate, intracontinental subduction is a sustainable process and is accompanied with atypical deformation pattern and melting process of the metasomatized mantle.

Perhaps the most interesting and striking result is that, regardless of the parameters used in the different models, melting occurs without the necessity of slab break-off, slab retreat, fluid transfer, or deep heat advection: It occurs during the fast downwelling of the metasomatized mantle corner indented by the southward advancing Songpan-Ganze slab. Since the metasomatized mantle is less dense than the underlying asthenosphere, this downwelling is not gravity driven: It is forced by the horizontal, convergent forces and is presumably only made possible by the very low viscosity fixed for the metasomatized mantle. This very distinctive type of deformation could therefore be specific to H₂O- and CO₂-rich peridotites, where the presence of phlogopite, carbonates, and “wet” anhydrous minerals greatly reduces the viscosity of the mantle (Figure 7). Mantle downwelling is not sufficient for melting to occur: The *P-T* paths of particles inside the downwelling mantle never cross the solidus of a hydrated peridotite (Figure 9c, blue curve; Falloon and Green, 1990). Melting is only made possible by the strong deflection of the solidus of carbonated peridotites (Figure 9c, black curve; Wallace & Green, 1988) toward lower temperatures at about 20 kbars (“carbonate ledge”; Hammouda & Keshav, 2015).

In all the models run, two distinct melting events systematically occur in 30 Ma of convergence. In the reference model, they occur about 15 Ma apart from each other (Figure 9a): This temporality of magmatism is exactly the same as observed between the Xialaxiu (~ 50 Ma) and Nangqian (~ 35 Ma) basins.

The expected volcanism at the surface of the model shows an increase in the distance to the suture from the first (70–120 km to the suture) to the second melting event (100–170 km to the suture; Figure 9b). These

distances differ from the location of magmatic outcrops in the Xialaxiu and Nangqian basins (at 50 and 100 km to the Jinsha suture; Figure 1b), but they do not consider coeval and later crustal shortening (at least 61 km; Spurlin et al., 2005). Moreover, the rates of southward migration of the magmatism are still coherent with that observed (3–5 mm/year) and thus directly reflect the imposed convergence rate and subduction angle, as for “classical” arc magmatism.

It is nevertheless striking that the reference model correctly reproduces both the observed temporality of magmatism and the observed rate of southward migration of the magmatism, since these results appear very sensitive to the initial parameters used (Text S3). This suggests that the rheology of the Qiangtang lithospheric mantle and the geometry of the Jinsha suture considered in the reference model best explain the observations. A rectangular geometry is not oversimplified in the case of Tibetan continental blocks: Most Mesozoic sutures inherited from the final closure of the Paleo-Tethys are today reactivated as large-scale vertical strike-slip faults probably deeply rooted in the lithosphere (Tapponnier & Molnar, 1976). The Jinsha Suture, of interest here, has indeed been imaged in Western Tibet by receiver functions tomography as drawing a sharp and vertical contact between the Songpan-Ganze (Tianshuihai) and Qiangtang terranes (Wittlinger et al., 2004).

5.3.3. A Too Localized Deformation: The Need for Other Intracontinental Subductions

Our reference model correctly reproduces the present-day crustal thickness imaged beneath northern Qiangtang (~66 km) but only up to 150 km south of the Jinsha suture zone. Thickening of the whole Eastern and Central Tibet therefore requires either a stronger coupling, through a more resistant metasomatized mantle rheology (of the R1 model type, Figure S3 and Table S8), or complementary thickening processes, such as a similar reactivation of other Tibetan sutures (e.g., Longmu Co and Bangong) as intracontinental subductions throughout the Cenozoic (Guillot & Replumaz, 2013; Tapponnier et al., 2001). Although well beyond the scope of our study, the discovery of trace element and isotopic fingerprints of carbonated metasomatism in the Miocene ultrapotassic volcanic rocks from the southwestern Lhasa terrane (Figure 1a; Liu et al., 2015) suggest that comparable processes of ancient mantle metasomatism may indeed be also envisaged in the southwestern part of the Tibetan Plateau.

Finally, our 2-D numerical model does not allow to study the behavior of the intracontinental subduction along-strike, and in particular the lateral transition to transpressive tectonics observed in the Eastern Collision Zone (Wang et al., 2001).

5.3.4. Age of the Subduction Initiation

Thermo-mechanical modeling also addresses the question of the initiation of Cenozoic shortening in Eastern/Central Tibet: Whereas it is commonly admitted to have started by Eocene times due to the far-field effect of the 55 ± 10 Ma India-Asia collision (Pitard et al., 2018; Replumaz et al., 2013; Tapponnier et al., 2001), there are some geological evidence of shortening throughout the Tibetan Plateau during Early Cretaceous times (Airaghi, 2017; Kapp, DeCelles, Leier, et al. 2007; Kapp, DeCelles, Gehrels, et al. 2007; Leloup et al., 2012; Yin et al., 2008). Melting in the models appears 5 to 18 Ma after the initiation of the convergence (Figures 9 and S3). By analogy, the *circa* 50 Ma volcanism in Xialaxiu would imply that the reactivation of the Jinsha suture started between 68 and 55 Ma, that is, 3 to 23 Ma before the India-Asia collision. Our models thus suggest that the building of the Tibetan Plateau slightly predated the India-Asia collision and was more powered by the regional asthenospheric mantle convection beneath the India-Eurasia plate system (Becker & Faccenna, 2011; Sternai et al., 2016; Jolivet et al., 2018) than by the sole collision of the Indian and Asian lithospheres.

5.4. Seismological Consequences of a Hydrated and Carbonated Eastern Tibetan Mantle

The present-day structure of the Tibetan lithosphere is assessed by geophysical studies. Teleseismic tomography reveal low *P*-wave velocity anomalies in the mantle lithosphere (Lei & Zhao, 2016; Li et al., 2008; Replumaz et al., 2013; Wang et al., 2019), notably beneath the Eastern Qiangtang and Songpan-Ganze terranes, but with great variations, even between the most recent models, of the lateral and depth extent of the anomalies (compare, e.g., Lei & Zhao, 2016; Wang et al., 2019). This low-velocity layer has been widely interpreted as a thermal anomaly indicative of a thinned lithospheric mantle (Liang et al., 2012; Tunini et al., 2016; Vozar et al., 2014). However, *S*-wave velocities, which are more sensitive to temperature than to composition, and thus more adequate to map the lithosphere thickness variations (Priestley & McKenzie, 2006), are not slowed and rather suggest a thick lithosphere (~260 km) beneath the whole Tibet Plateau (McKenzie & Priestley, 2008). Finally, receiver functions profiles show the presence of several interfaces (converters) between 180- and 200-km depth across the Tibet Plateau, suggesting a southward subduction of the Asian

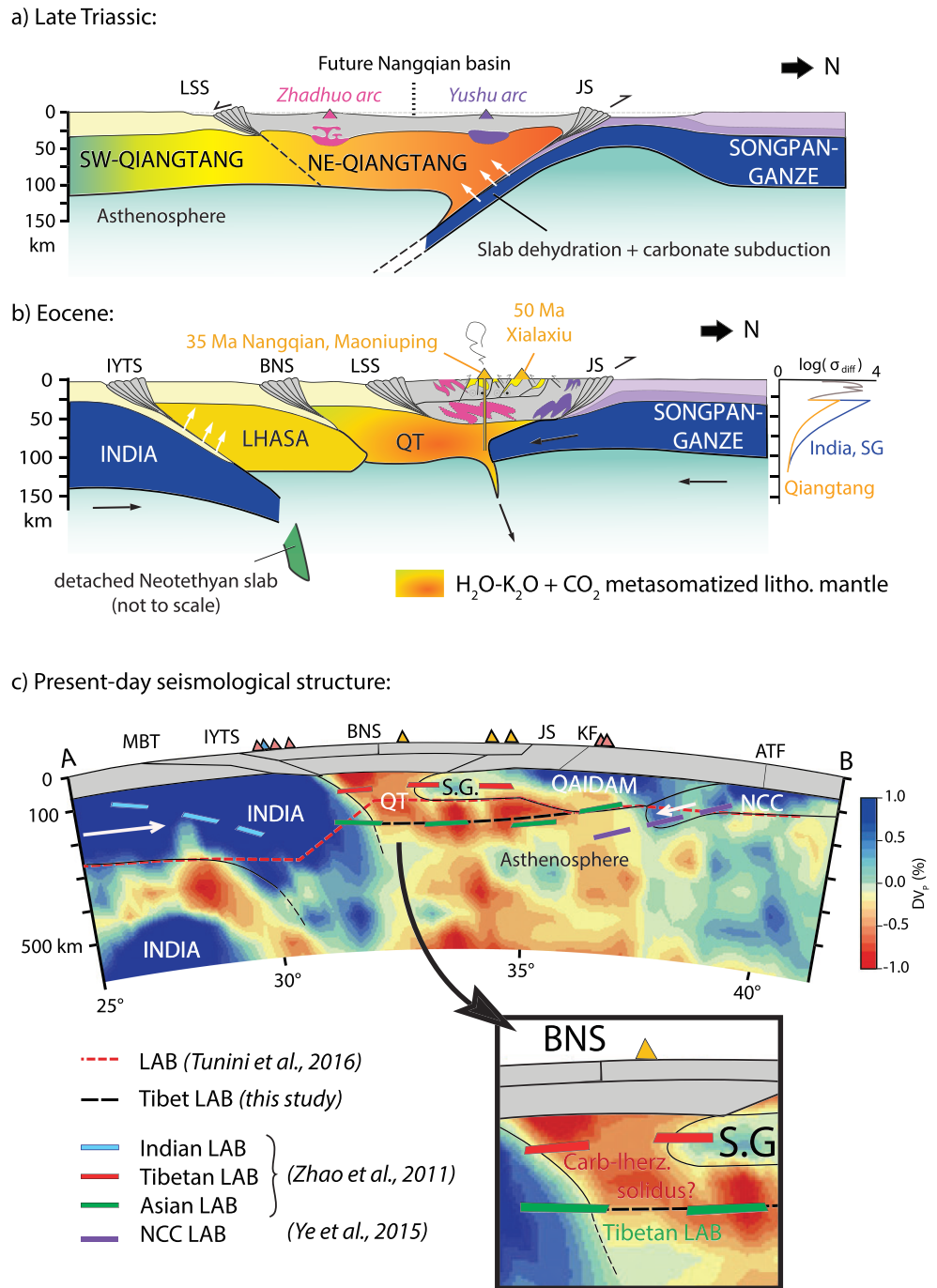


Figure 10. Three-stage inheritance of the Pre-Cenozoic H₂O-CO₂ mantle metasomatism over the rheology and magmatism in Eastern-Central Tibet. (a) Metasomatism of the subcontinental lithospheric mantle of the Qiangtang block during the late stages of the Paleo-Tethys closure. (b) Cenozoic uplift and potassic-carbonatitic magmatism, by indentation of the Songpan-Ganze lithosphere into the weakened Qiangtang mantle along the reactivated Jinsha Suture. Inset: corresponding lithospheric strength profiles of the Indian, Songpan-Ganze (SG), and Qiangtang lithospheric mantles. (c) Present-day low P-wave velocity zone beneath Eastern-Central Tibet, reinterpreted here as fossil metasomatic domains of the Tibetan lithosphere, rather than as asthenospheric mantle. The location of the A-B seismological transect (section D of Replumaz et al., 2013) is indicated on Figure 1a. Our Tibetan lithosphere-asthenosphere boundary (LAB) corresponds to the Asian LAB of Zhao et al. (2011) imaged by S receiver function. The Tibetan LAB of these authors has no equivalent in our model, but its depth (100–120 km) fit the location of a carbonated peridotite solidus under the Cold Geotherm we use in our study (Figure 5d). The LAB of Tunini et al. (2016) is indicated for comparison. Abbreviations are the same as in Figure 1, plus LH = Lhasa; QT = Qiangtang; SG = Songpan-Ganze; QA = Qaidam; NCC = North China Craton.

lithosphere and the stacking of Tibetan and Asian lithospheres beneath the northern and central parts of the Plateau (Kind et al., 2002; Wittlinger et al., 2004; Zhao et al., 2010, 2011). These conflicting interpretations of the geophysical data could be reconciled by considering that the slow seismic wave velocities may, alternatively, record a geochemical rather than thermal anomaly in the Tibetan lithospheric mantle (Zhang et al., 2014).

Indeed, by modeling the addition of phlogopite and magnesian carbonate to a Tibetan lithospheric mantle of normal thickness (150 km) under a normal (“cold”) continental geotherm, we are able to reproduce the present-day V_p anomaly (Figure 6a; Li et al., 2008; Replumaz et al., 2013), the shear wave velocity profile (Figure 6b; Vozar et al., 2014), and the low mantle density (Figure 6c) inferred from the topography and gravity data of the Tibet Plateau (Tunini et al., 2016). The persistence up to present day of a metasomatic mineralogy in the lithospheric mantle of Eastern-Central Tibet can thus explain the geophysical observations without recourse to lithospheric thinning and associated asthenospheric upwelling.

The A-B cross section shown in Figure 1a has been recently used for an integrated petrological-geophysical modeling of the Tibetan lithosphere (Tunini et al., 2016). We propose here an alternative interpretation of the corresponding V_p tomographic cross section (Replumaz et al., 2013), where the slow P -wave anomaly beneath Central Tibet images the lithospheric mantle of the Qiangtang terrane, of normal thickness (~150–200 km), but having preserved its old, inherited metasomatic mineralogy (Figure 10c). A similar relationship between low seismic velocities in the upper mantle and carbonated metasomatism has been proposed for the Mediterranean region (Peccerillo et al., 2008), the North China Craton and Western Tibet (Zhang et al., 2014).

Such reinterpretation of the seismic data is not by itself in conflict with the data requiring an elevated crustal thermal gradient in Tibet (Hacker et al., 2014; Mechie et al., 2004; Wang et al., 2016; Yang et al., 2012). As modeled by McKenzie and Priestley (2008) and McKenzie et al. (2019), radiogenic heat production alone, inside the overthickened Tibetan crust, would result in very high midcrustal temperatures, with no need for an elevated heat flux from the mantle and with Moho temperatures only about 700°C, as in our “cold” geotherm (see Figure 7 of McKenzie & Priestley, 2008, at $t = 55$ Ma).

Actually, McKenzie and Priestley (2008)’s model also shows that this warm crust may eventually heat the underlying uppermost lithospheric mantle. Indeed, although we only focused on metasomatism, we cannot exclude that the present-day seismic signature of the first hundred km of the Tibetan lithospheric mantle may result from an interplay between metasomatic and thermal effects.

6. Conclusion

Based on the occurrence of mantle-derived hydrated and carbonated minerals in Eocene potassic rocks from the Eastern Tibetan Plateau, and drawing a parallel with the Eastern Collision Zone carbonatitic-potassic associations, we reinterpret the low P -wave velocity anomaly beneath the Tibetan Plateau as being the expression of its peculiar composition due to ancient H_2O - CO_2 mantle metasomatism, rather than the expression of a thinned lithosphere. We show that such metasomatism lowered the density, the viscosity, and the melting temperature of the lithospheric mantle. These characteristics allow to reconcile the Cenozoic syn-contractual magmatism and uplift of the Eastern Tibetan Plateau with an intracontinental subduction of the Songpan-Ganze terrane along the reactivated Jinsha suture, thanks to a very specific type of coeval melting and deformation of the H_2O - and CO_2 -metasomatized mantle during this subduction, with no need for slab break-off, slab retreat, and fluid transfer nor deep heat advection. In a broader perspective, the widespread evidence of subcontinental lithospheric mantle metasomatism (Downes, 2001; Ducea et al., 2005) implies that these processes should be considered at other periods and in other collisional systems and underlines the importance of the rheological inheritance for the interpretation of geophysical data and associated inferences on geodynamic processes.

Data Availability Statement

Geochemical data are archived in the PANGAEA database (Table S1: <https://doi.org/10.1594/PANGAEA.910772>, Goussin et al., 2020b; Table S2: <https://doi.org/10.1594/PANGAEA.910790>, 2020a). All data and modeling parameters can be found in the supporting information.

Acknowledgments

This project was funded by the Agence Nationale de la Recherche (ANR-13-BS06-012-01) and the Labex OSUG@2020 (ANR10 LABX56). G. D.-N. acknowledges funding from ERC Grant MAGIC 649081. Z. G. contributed to the general organization of the project; F. G., S. G., P. R., A. R., and G. D.-N. participated to the field work and sample collection; F. G., C. C., and P. B. performed the petrographic and geochemical analysis; F. G. did the pseudosection modeling and the density and seismic velocity calculations; F. G., and K. S. made the lithospheric strength calculations; F. G., C. C., N. R., and S. G. wrote the manuscript; all authors discussed the results and commented the manuscript. All authors declare no competing financial interests.

References

Airaghi, L. (2017). A petro-chronological study of the Longmen Shan Thrust Belt (Eastern Tibet) : Geological inheritance and implication for the present geodynamics, Université Grenoble Alpes.

Becker, T. W., & Faccenna, C. (2011). Mantle conveyor beneath the Tethyan Collisional Belt. *Earth and Planetary Science Letters*, 310(3), 453–461. <https://doi.org/10.1016/j.epsl.2011.08.021>

Bina, C. R., & Helffrich, G. R. (1992). Calculation of elastic properties from thermodynamic equation of state principles. *Annual Review of Earth and Planetary Sciences*, 20(1), 527–552. <https://doi.org/10.1146/annurev.ea.20.050192.002523>

Bouilhol, P., Magni, V., van Hunen, J., & Kaislaniemi, L. (2015). A numerical approach to melting in warm subduction zones. *Earth and Planetary Science Letters*, 411, 37–44. <https://doi.org/10.1016/j.epsl.2014.11.043>

Bouvier, A., Vervoort, J. D., & Patchett, P. J. (2008). The Lu-Hf and Sm-Nd isotopic composition of CHUR: Constraints from unequilibrated chondrites and implications for the bulk composition of terrestrial planets. *Earth and Planetary Science Letters*, 273(1-2), 48–57. <https://doi.org/10.1016/j.epsl.2008.06.010>

Bystricky, M., Lawlis, J., Mackwell, S., Heidelbach, F., & Raterron, P. (2016). High-temperature deformation of enstatite aggregates. *Journal of Geophysical Research: Solid Earth*, 121, 6384–6400. <https://doi.org/10.1002/2016JB013011>

Bystricky, M., & Mackwell, S. (2001). Creep of dry clinopyroxene aggregates. *Journal of Geophysical Research*, 106(B7), 13,443–13,454. <https://doi.org/10.1029/2001JB000333>

Chauvel, C., Bureau, S., & Poggi, C. (2011). Comprehensive chemical and isotopic analyses of basalt and sediment reference materials. *Geostandards and Geoanalytical Research*, 35, 125–143. <https://doi.org/10.1111/j.1751-908X.2010.00086.x>

Cheng, Z., & Guo, Z. (2017). Post-collisional ultrapotassic rocks and mantle xenoliths in the Sailipu Volcanic Field of Lhasa Terrane, South Tibet: Petrological and geochemical constraints on mantle source and geodynamic setting. *Gondwana Research*, 46, 17–42. <https://doi.org/10.1016/j.gr.2017.02.008>

Chung, S. L., Chu, M. F., Zhang, Y., Xie, Y., Lo, C. H., Lee, T. Y., et al. (2005). Tibetan tectonic evolution inferred from spatial and temporal variations in post-collisional magmatism. *Earth-Science Reviews*, 68(3), 173–196.

Clark, M. K., Farley, K. A., Zheng, D., Wang, Z., & Duvall, A. R. (2010). Early Cenozoic faulting of the Northern Tibetan Plateau margin from apatite (U-Th)/He ages. *Earth and Planetary Science Letters*, 296(1–2), 78–88. <https://doi.org/10.1016/j.epsl.2010.04.051>

Condamine, P., & Médard, E. (2014). Experimental melting of phlogopite-bearing mantle at 1 GPa: Implications for potassic magmatism. *Earth and Planetary Science Letters*, 397, 80–92. <https://doi.org/10.1016/j.epsl.2014.04.027>

Connolly, J. A. D., & Kerrick, D. M. (2002). Metamorphic controls on seismic velocity of subducted oceanic crust at 100–250 km depth. *Earth and Planetary Science Letters*, 204(1), 61–74.

Crameri, F., Tackley, P. J., Meilick, I., Gerya, T. V., & Kaus, B. J. P. (2012). A free plate surface and weak oceanic crust produce single-sided subduction on Earth. *Geophysical Research Letters*, 39, L03306. <https://doi.org/10.1029/2011GL050046>

Deines, P. (1989). *Stable isotope variations in carbonatites*, Carbonatites: Genesis and Evolution (pp. 301–359). London: Unwin Hyman.

Dimanov, A., & Dresen, G. (2005). Rheology of synthetic anorthite-diopside aggregates: Implications for ductile shear zones. *Journal of Geophysical Research*, 110, B07203. <https://doi.org/10.1029/2004JB003431>

Ding, L., Kapp, P., Yue, Y., & Lai, Q. (2007). Postcollisional calc-alkaline lavas and xenoliths from the southern Qiangtang Terrane, Central Tibet. *Earth and Planetary Science Letters*, 254(1–2), 28–38. <https://doi.org/10.1016/j.epsl.2006.11.019>

Downes, H. (2001). Formation and modification of the shallow sub-continental lithospheric mantle: A review of geochemical evidence from ultramafic xenolith suites and tectonically emplaced ultramafic massifs of western and central Europe. *Journal of Petrology*, 42(1), 233–250.

Ducea, M. N., Saleeby, J., Morrison, J., & Valencia, V. A. (2005). Subducted carbonates, metasomatism of mantle wedges, and possible connections to diamond formation: An example from California. *American Mineralogist*, 90(5-6), 864–870. <https://doi.org/10.2138/am.2005.1670>

England, P., & Houseman, G. (1989). Extension during continental convergence, with application to the Tibetan Plateau. *Journal of Geophysical Research*, 94(B12), 17,561–17,579. <https://doi.org/10.1029/JB094iB12p17561>

Falloon, T. J., & Green, D. H. (1990). Solidus of carbonated fertile peridotite under fluid-saturated conditions. *Geology*, 18(3), 195–199. [https://doi.org/10.1130/0091-7613\(1990\)018<0195:SOCFPU>2.3.CO;2](https://doi.org/10.1130/0091-7613(1990)018<0195:SOCFPU>2.3.CO;2)

Franzolin, E., Schmidt, M. W., & Poli, S. (2011). Ternary Ca-Fe-Mg carbonates: Subsolvus phase relations at 3.5 GPa and a thermodynamic solid solution model including order/disorder. *Contributions to Mineralogy and Petrology*, 161(2), 213–227. <https://doi.org/10.1007/s00410-010-0527-x>

Fritschle, T., Prelević, D., Foley, S. F., & Jacob, D. E. (2013). Petrological characterization of the mantle source of Mediterranean lamproites: Indications from major and trace elements of phlogopite. *Chemical Geology*, 353, 267–279. <https://doi.org/10.1016/j.chemgeo.2012.09.006>

Goussin, F., Cordier, C., Riel, N., Guillot, S., Boulvais, P., Roperch, P., et al. (2020a). Representative major element compositions of clinopyroxenes and phlogopites from ultrapotassic rocks from Nangqian basin (Eastern Tibet). <https://doi.org/10.1594/PANGAEA.910790>

Goussin, F., Cordier, C., Riel, N., Guillot, S., Boulvais, P., Roperch, P., et al. (2020b). Whole-rock major and trace elements data, and whole-rock and carbonate isotope data, for the potassic and ultrapotassic rocks from Nangqian basin (Eastern Tibet). <https://doi.org/10.1594/PANGAEA.910772>

Griffin, W. L., O'Reilly, S. Y., Afonso, J. C., & Begg, G. C. (2009). The composition and evolution of lithospheric mantle: A re-evaluation and its tectonic implications. *Journal of Petrology*, 50(7), 1185–1204. <https://doi.org/10.1093/ptrology/egn033>

Guillot, S., & Replumaz, A. (2013). Importance of continental subductions for the growth of the Tibetan Plateau. *Bulletin de la Société Géologique de France*, 184(3), 199–223.

Guo, Z. (2006). Post-Collisional, Potassic and ultrapotassic magmatism of the northern Tibetan Plateau: Constraints on characteristics of the mantle source, geodynamic setting and uplift mechanisms. *Journal of Petrology*, 47(6), 1177–1220. <https://doi.org/10.1093/ptrology/egl007>

Hacker, B. R., Ritzwoller, M. H., & Xie, J. (2014). Partially melted, mica-bearing crust in Central Tibet. *Tectonics*, 33, 1408–1424. <https://doi.org/10.1002/2014TC003545>

Hammouda, T., & Keshav, S. (2015). Melting in the mantle in the presence of carbon: Review of experiments and discussion on the origin of carbonatites. *Chemical Geology*, 418, 171–188. <https://doi.org/10.1016/j.chemgeo.2015.05.018>

Holland, T. J. B., & Powell, R. (1998). An internally consistent thermodynamic data set for phases of petrological interest. *Journal of Metamorphic Geology*, 16(3), 309–343.

Holyoke, C. W., Kronenberg, A. K., Newman, J., & Ulrich, C. (2014). Rheology of magnesite. *Journal of Geophysical Research: Solid Earth*, 119, 6534–6557. <https://doi.org/10.1002/2013JB010541>

- Horton, B. K., Yin, A., Spurlin, M. S., Zhou, J., & Wang, J. (2002). Paleocene-eocene syncontractional sedimentation in narrow, lacustrine-dominated basins of east-central Tibet. *GSA Bulletin*, *114*(7), 771–786.
- Hou, Z., Tian, S., Yuan, Z., Xie, Y., Yin, S., Yi, L., et al. (2006). The Himalayan collision zone carbonatites in western Sichuan, SW China: Petrogenesis, mantle source and tectonic implication. *Earth and Planetary Science Letters*, *244*(1–2), 234–250. <https://doi.org/10.1016/j.epsl.2006.01.052>
- Hou, Z., Wang, L. Q., Khin, Z., Mo, X. X., Wang, M., Li, D., & Pan, G. (2003). Post-collisional crustal extension setting and VHMS mineralization in the Jinshajiang Orogenic Belt, southwestern China. *Ore Geology Reviews*, *22*(3–4), 177–199. [https://doi.org/10.1016/S0169-1368\(02\)00141-5](https://doi.org/10.1016/S0169-1368(02)00141-5)
- Huang, X. L., Niu, Y., Xu, Y. G., Chen, L. L., & Yang, Q. J. (2010). Mineralogical and geochemical constraints on the petrogenesis of post-collisional potassic and ultrapotassic rocks from western Yunnan, SW China. *Journal of Petrology*, *51*(8), 1617–1654. <https://doi.org/10.1093/ptrology/egq032>
- Huet, B., Yamato, P., & Grasemann, B. (2014). The minimized power geometric model: An analytical mixing model for calculating polyphase rock viscosities consistent with experimental data. *Journal of Geophysical Research: Solid Earth*, *119*, 3897–3924. <https://doi.org/10.1002/2013JB010453>
- Irving, A. J., & Frey, F. A. (1984). Trace element abundances in megacrysts and their host basalts: Constraints on partition coefficients and megacryst genesis. *Geochimica et Cosmochimica Acta*, *48*(6), 1201–1221. [https://doi.org/10.1016/0016-7037\(84\)90056-5](https://doi.org/10.1016/0016-7037(84)90056-5)
- Jiang, Y. H., Jiang, S. Y., Ling, H. F., & Dai, B. Z. (2006). Low-degree melting of a metasomatized lithospheric mantle for the origin of Cenozoic Yulong monzogranite-porphiry, East Tibet: Geochemical and Sr-Nd-Pb-Hf isotopic constraints. *Earth and Planetary Science Letters*, *241*(3–4), 617–633. <https://doi.org/10.1016/j.epsl.2005.11.023>
- Jiménez-Munt, I., & Platt, J. P. (2006). Influence of mantle dynamics on the topographic evolution of the Tibetan Plateau: Results from numerical modeling. *Tectonics*, *25*, TC6002. <https://doi.org/10.1029/2006TC001963>
- Jolivet, L., Faccenna, C., Becker, T., Tesauro, M., Sternai, P., & Bouilhol, P. (2018). Mantle flow and deforming continents: From India-Asia convergence to Pacific subduction. *Tectonics*, *37*, 2887–2914. <https://doi.org/10.1029/2018TC005036>
- Kapp, P., DeCelles, P. G., Gehrels, G. E., Heizler, M., & Ding, L. (2007). Geological records of the Lhasa-Qiangtang and Indo-Asian collisions in the Nima Area of Central Tibet. *Geological Society of America Bulletin*, *119*(7–8), 917–933.
- Kapp, P., DeCelles, P. G., Leier, A. L., Fabijanic, J. M., He, S., Pullen, A., et al. (2007). The Gangdese retroarc thrust belt revealed. *GSA Today*, *17*(7), 4.
- Karato, S. i. (2010). Rheology of the deep upper mantle and its implications for the preservation of the continental roots: A review. *Tectonophysics*, *481*(1), 82–98. <https://doi.org/10.1016/j.tecto.2009.04.011>
- Karato, S. I., & Jung, H. (2003). Effects of pressure on high-temperature dislocation creep in olivine. *Philosophical Magazine*, *83*(3), 401–414. <https://doi.org/10.1080/0141861021000025829>
- Kawazoe, T., Karato, S. i., Otsuka, K., Jing, Z., & Mookherjee, M. (2009). Shear deformation of dry polycrystalline olivine under deep upper mantle conditions using a Rotational Drickamer Apparatus (RDA). *Physics of the Earth and Planetary Interiors*, *174*(1), 128–137. <https://doi.org/10.1016/j.pepi.2008.06.027>
- Kind, R., Yuan, X., Saul, J., Nelson, D., Sobolev, S. V., Mechie, J., et al. (2002). Seismic images of crust and upper mantle beneath Tibet: Evidence for Eurasian Plate Subduction. *Science*, *298*(5596), 1219–1221.
- Kohlstedt, D. L., Evans, B., & Mackwell, S. J. (1995). Strength of the lithosphere: Constraints imposed by laboratory experiments. *Journal of Geophysical Research*, *100*(B9), 17,587–17,602. <https://doi.org/10.1029/95JB01460>
- Kronenberg, K., & Pinkston (1990). Basal slip and mechanical anisotropy of biotite.
- Lai, S. c., Qin, J. f., & Khan, J. (2014). The carbonated source region of Cenozoic mafic and ultra-mafic lavas from western Qinling: Implications for eastern mantle extrusion in the northeastern margin of the Tibetan Plateau. *Gondwana Research*, *25*(4), 1501–1516. <https://doi.org/10.1016/j.gr.2013.05.019>
- Le Maitre, R. W., Streckeisen, A., Zanettin, B., Le Bas, M. J., Bonin, B., Bateman, P., & Keller, J. (2002). *Igneous rocks. A classification and glossary of terms. Recommendations of the IUGS Subcommittee on the Systematics of Igneous Rocks*. Cambridge: Cambridge University Press.
- Lei, J., & Zhao, D. (2016). Teleseismic P-wave tomography and mantle dynamics beneath eastern Tibet. *Geochemistry, Geophysics, Geosystems*, *17*, 1861–1884. <https://doi.org/10.1002/2016GC006262>
- Leloup, P., Arnaud, N., Mahéo, G., Paquette, J., Guillot, S., Valli, F., et al. (2012). Successive deformation episodes along the Lungmu Co Zone, west-central Tibet. *Gondwana Research*, *21*(1), 37–52. <https://doi.org/10.1016/j.gr.2011.07.026>
- Li, L., Long, H., Raterron, P., & Weidner, D. (2006). Plastic flow of pyrope at mantle pressure and temperature. *American Mineralogist*, *91*(4), 517–525. <https://doi.org/10.2138/am.2006.1913>
- Li, C., van der Hilst, R. D., Meltzer, A. S., & Engdahl, E. R. (2008). Subduction of the Indian lithosphere beneath the Tibetan Plateau and Burma. *Earth and Planetary Science Letters*, *274*(1–2), 157–168. <https://doi.org/10.1016/j.epsl.2008.07.016>
- Li, C., Zhai, Q., Dong, Y., & Huang, X. (2006). Discovery of eclogite and its geological significance in Qiangtang Area, Central Tibet. *Chinese Science Bulletin*, *51*(9), 1095–1100. <https://doi.org/10.1007/s11434-006-1095-3>
- Liang, X., Sandvol, E., Chen, Y. J., Hearn, T., Ni, J., Klemperer, S., et al. (2012). A complex Tibetan upper mantle: A fragmented Indian slab and no south-verging subduction of Eurasian lithosphere. *Earth and Planetary Science Letters*, *333–334*(101–111). <https://doi.org/10.1016/j.epsl.2012.03.036>
- Liu, C. Z., Wu, F. Y., Chung, S. L., & Zhao, Z. D. (2011). Fragments of hot and metasomatized mantle lithosphere in middle Miocene ultrapotassic lavas, southern Tibet. *Geology*, *39*(10), 923–926.
- Liu, D., Zhao, Z., Zhu, D. C., Niu, Y., Widom, E., Teng, F. Z., et al. (2015). Identifying mantle carbonatite metasomatism through Os–Sr–Mg isotopes in Tibetan ultrapotassic rocks. *Earth and Planetary Science Letters*, *430*, 458–469. <https://doi.org/10.1016/j.epsl.2015.09.005>
- Lu, L., Zhang, K. J., Yan, L. L., Jin, X., & Zhang, Y. X. (2017). Was Late Triassic Tanggula granitoid (Central Tibet, Western China) a product of melting of underthrust Songpan-Ganzi Flysch sediments?: Genesis of Tanggula granitoid. *Tectonics*, *36*, 902–928. <https://doi.org/10.1002/2016TC004384>
- Mattoli, G. S., Baker, M. B., Rutter, M. J., & Stolper, E. M. (1989). Upper mantle oxygen fugacity and its relationship to metasomatism. *The Journal of Geology*, *97*(5), 521–536. <https://doi.org/10.1086/629332>
- McDonough, W. F., & Rudnick, R. L. (1999). Mineralogy and composition of the upper mantle. *Reviews in Mineralogy*, *37*, 139–164.
- McDonough, W. F., & Sun, S. S. (1995). The composition of the Earth. *Chemical Geology*, *120*(3–4), 223–253.
- McKenzie, D., McKenzie, J., & Fairhead, D. (2019). The mechanical structure of Tibet. *Geophysical Journal International*, *217*(2), 950–969. <https://doi.org/10.1093/gji/ggz052>
- McKenzie, D., & Priestley, K. (2008). The influence of lithospheric thickness variations on continental evolution. *Lithos*, *102*(1–2), 1–11. <https://doi.org/10.1016/j.lithos.2007.05.005>

- Mechie, J., Sobolev, S. V., Ratschbacher, L., Babeyko, A. Y., Bock, G., Jones, A. G., et al. (2004). Precise temperature estimation in the Tibetan crust from seismic detection of the α - β quartz transition. *Geology*, 32(7), 601–604. <https://doi.org/10.1130/G20367.1>
- Meyer, B., Tapponnier, P., Bourjot, L., Métyvier, F., Gaudemer, Y., Peltzer, G., et al. (1998). Crustal thickening in Gansu-Qinghai, lithospheric mantle subduction, and oblique, strike-slip controlled growth of the Tibet Plateau. *Geophysical Journal International*, 135(1), 1–47. <https://doi.org/10.1046/j.1365-246X.1998.00567.x>
- Mo, X., Zhao, Z., Deng, J., Flower, M., Yu, X., Luo, Z., et al. (2006). Petrology and geochemistry of postcollisional volcanic rocks from the Tibetan Plateau: Implications for lithosphere heterogeneity and collision-induced asthenospheric mantle flow, *Special Paper 409: Postcollisional Tectonics and Magmatism in the Mediterranean Region and Asia* (vol. 409, pp. 507–530): Geological Society of America.
- Molnar, P., England, P., & Martinod, J. (1993). Mantle dynamics, uplift of the Tibetan Plateau, and the Indian Monsoon. *Reviews of Geophysics*, 31(4), 357. <https://doi.org/10.1029/93RG02030>
- Moresi, L., Quenette, S., Lemiale, V., Mériaux, C., Appelbe, B., & Mühlhaus, H. B. (2007). Computational approaches to studying non-linear dynamics of the crust and mantle. *Physics of the Earth and Planetary Interiors*, 163(1–4), 69–82. <https://doi.org/10.1016/j.pepi.2007.06.009>
- Newton, R. C., Charlu, T. V., & Kleppa, O. J. (1980). Thermochemistry of the high structural state plagioclases. *Geochimica et Cosmochimica Acta*, 44(7), 933–941.
- Ohuchi, T., Karato, S. i., & Fujino, K. (2011). Strength of single-crystal orthopyroxene under lithospheric conditions. *Contributions to Mineralogy and Petrology*, 161(6), 961–975. <https://doi.org/10.1007/s00410-010-0574-3>
- Peccerillo, A., Panza, G. F., Aoudia, A., & Frezzotti, M. L. (2008). Relationships between magmatism and lithosphere-asthenosphere structure in the western Mediterranean and implications for geodynamics. *Rendiconti Lincei*, 19(4), 291–309. <https://doi.org/10.1007/s12210-008-0020-x>
- Pitard, P., Replumaz, A., Funicello, F., Husson, L., & Faccenna, C. (2018). Mantle kinematics driving collisional subduction: Insights from analogue modeling. *Earth and Planetary Science Letters*, 502, 96–103. <https://doi.org/10.1016/j.epsl.2018.08.050>
- Powell, R., & Holland, T. (1999). Relating formulations of the thermodynamics of mineral solid solutions: Activity modeling of pyroxenes, amphiboles, and micas. *American Mineralogist*, 84(1–2), 1–14. <https://doi.org/10.2138/am-1999-1-201>
- Priestley, K., & McKenzie, D. (2006). The thermal structure of the lithosphere from shear wave velocities. *Earth and Planetary Science Letters*, 244(1), 285–301. <https://doi.org/10.1016/j.epsl.2006.01.008>
- Ranalli, G. (1997). Rheology of the lithosphere in space and time. *Geological Society, London, Special Publications*, 121(1), 19–37. <https://doi.org/10.1144/GSL.SP.1997.121.01.02>
- Replumaz, A., Funicello, F., Reitano, R., Faccenna, C., & Balon, M. (2016). Asian collisional subduction: A key process driving formation of the Tibetan Plateau. *Geology*, 44(11), 943–946. <https://doi.org/10.1130/G38276.1>
- Replumaz, A., Guillot, S., Villaseñor, A., & Negrodo, A. M. (2013). Amount of Asian lithospheric mantle subducted during the India/Asia collision. *Geodynamics Research*, 24(3–4), 936–945. <https://doi.org/10.1016/j.gr.2012.07.019>
- Roger, F., Jolivet, M., & Malavieille, J. (2010). The tectonic evolution of the Songpan-Garzê (North Tibet) and adjacent areas from Proterozoic to present: A synthesis. *Journal of Asian Earth Sciences*, 39(4), 254–269. <https://doi.org/10.1016/j.jseas.2010.03.008>
- Roger, F., Tapponnier, P., Arnaud, N., Schärer, U., Brunel, M., Zhiqin, X., & Jingsui, Y. (2000). An Eocene magmatic belt across Central Tibet: Mantle subduction triggered by the Indian collision? *Terra Nova*, 12(3), 102–108. <https://doi.org/10.1046/j.1365-3121.2000.123282.x>
- She, Z., Ma, C., Mason, R., Li, J., Wang, G., & Lei, Y. (2006). Provenance of the Triassic Songpan-Ganzi Flysch, West China. *Chemical Geology*, 231(1–2), 159–175. <https://doi.org/10.1016/j.chemgeo.2006.01.001>
- Shinevar, W. J., Behn, M. D., & Hirth, G. (2015). Compositional dependence of lower crustal viscosity. *Geophysical Research Letters*, 42(20), 8333–8340. <https://doi.org/10.1002/2015GL065459>
- Spurlin, M. S., Yin, A., Horton, B. K., Zhou, J., & Wang, J. (2005). Structural evolution of the Yushu-Nangqian region and its relationship to syncollisional igneous activity, East-Central Tibet. *Geological Society of America Bulletin*, 117(9–10), 1293–1317.
- Sternai, P., Avouac, J. P., Jolivet, L., Faccenna, C., Gerya, T., Becker, T. W., & Menant, A. (2016). On the influence of the asthenospheric flow on the tectonics and topography at a collision-subduction transition zones: Comparison with the eastern Tibetan margin. *Journal of Geodynamics*, 100, 184–197. <https://doi.org/10.1016/j.jog.2016.02.009>
- Sun, H., Deng, W. M., & Zhang, Y. (2001). Petrogenesis of Cenozoic potassic volcanic rocks in the Nangqên Basin. *Acta Geologica Sinica - English Edition*, 75(1), 27–40. <https://doi.org/10.1111/j.1755-6724.2001.tb00504.x>
- Tapponnier, P., & Molnar, P. (1976). Slip-line field theory and large-scale continental tectonics. *Nature*, 264(5584), 319.
- Tapponnier, P., Zhiqin, X., Roger, F., Meyer, B., Arnaud, N., Wittlinger, G., & Jingsui, Y. (2001). Oblique stepwise rise and growth of the Tibet Plateau. *Science*, 294(5547), 1671–1677.
- Taylor, H. P., Frechen, J., & Degens, E. T. (1967). Oxygen and carbon isotope studies of carbonatites from the Laacher See District, West Germany and the Alnö District, Sweden. *Geochimica et Cosmochimica Acta*, 31(3), 407–430. [https://doi.org/10.1016/0016-7037\(67\)90051-8](https://doi.org/10.1016/0016-7037(67)90051-8)
- Tunini, L., Jiménez-Munt, I., Fernandez, M., Vergés, J., Villaseñor, A., Melchiorre, M., & Afonso, J. C. (2016). Geophysical-petrological model of the crust and upper mantle in the India-Eurasia collision zone: LITHOSPHERE OF INDIA-EURASIA COLLISION. *Tectonics*, 35, 1642–1669. <https://doi.org/10.1002/2016TC004161>
- Turcotte, D., & Schubert, G. (2014). *Geodynamics*. Cambridge: Cambridge University Press.
- Vozer, J., Jones, A. G., Fullea, J., Agius, M. R., Lebedev, S., Le Pape, F., & Wei, W. (2014). Integrated geophysical-petrological modeling of lithosphere-asthenosphere boundary in Central Tibet using electromagnetic and seismic data. *Geochemistry, Geophysics, Geosystems*, 15, 3965–3988. <https://doi.org/10.1002/2014GC005365>
- Wallace, M. E., & Green, D. H. (1988). An experimental determination of primary carbonatite magma composition. *Nature*, 335(6188), 343.
- Wang, Q., Hawkesworth, C. J., Wyman, D., Chung, S. L., Wu, F. Y., Li, X. H., et al. (2016). Pliocene-Quaternary crustal melting in central and northern Tibet and insights into crustal flow. *Nature Communications*, 7(1), 11888. <https://doi.org/10.1038/ncomms11888>
- Wang, X., Metcalfe, I., Jian, P., He, L., & Wang, C. (2000). The Jinshajiang-Ailaoshan suture zone, China: Tectonostratigraphy, age and evolution. *Journal of Asian Earth Sciences*, 18(6), 675–690.
- Wang, J. H., Yin, A., Harrison, T. M., Grove, M., Zhang, Y. Q., & Xie, G. H. (2001). A tectonic model for Cenozoic igneous activities in the Eastern Indo-Asian collision zone. *Earth and Planetary Science Letters*, 188(1–2), 123–133. [https://doi.org/10.1016/S0012-821X\(01\)00315-6](https://doi.org/10.1016/S0012-821X(01)00315-6)
- Wang, Z., Zhao, D., Gao, R., & Hua, Y. (2019). Complex subduction beneath the Tibetan Plateau: A slab warping model. *Physics of the Earth and Planetary Interiors*, 292, 42–54. <https://doi.org/10.1016/j.pepi.2019.04.007>
- Wei, C., & Powell, R. (2003). Phase relations in high-pressure metapelites in the system KFMASH (K₂O-FeO-MgO-Al₂O₃-SiO₂-H₂O) with application to natural rocks. *Contributions to Mineralogy and Petrology*, 145(3), 301–315.

- White, R. W., Powell, R., & Holland, T. J. B. (2001). Calculation of partial melting equilibria in the system Na₂O–CaO–K₂O–FeO–MgO–Al₂O₃–SiO₂–H₂O (NCKFMASH). *Journal of Metamorphic Geology*, *19*(2), 139–153.
- Williams, H. M. (2004). Nature of the source regions for post-collisional, potassic magmatism in southern and northern Tibet from geochemical variations and inverse trace element modelling. *Journal of Petrology*, *45*(3), 555–607. <https://doi.org/10.1093/petrology/egg094>
- Wittlinger, G., Vergne, J., Tapponnier, P., Farra, V., Poupinet, G., Jiang, M., et al. (2004). Teleseismic imaging of subducting lithosphere and Moho offsets beneath Western Tibet. *Earth and Planetary Science Letters*, *221*(1–4), 117–130. [https://doi.org/10.1016/S0012-821X\(03\)00723-4](https://doi.org/10.1016/S0012-821X(03)00723-4)
- Wu, C., Yin, A., Zusa, A. V., Zhang, J., Liu, W., & Ding, L. (2016). Pre-Cenozoic geologic history of the central and northern Tibetan Plateau and the role of Wilson cycles in constructing the Tethyan orogenic system. *Lithosphere*, *8*, 254–292. <https://doi.org/10.1130/L494.1>
- Wyllie, P. J., & Sekine, T. (1982). The formation of mantle phlogopite in subduction zone hybridization. *Contributions to Mineralogy and Petrology*, *79*(4), 375–380.
- Xia, L., Li, X., Ma, Z., Xu, X., & Xia, Z. (2011). Cenozoic volcanism and tectonic evolution of the Tibetan plateau. *Gondwana Research*, *19*(4), 850–866. <https://doi.org/10.1016/j.gr.2010.09.005>
- Xu, Y., Bi, X. W., Hu, R. Z., Chen, Y. w., Liu, H. q., & Xu, L. I. (2016). Geochronology and geochemistry of Eocene potassic felsic intrusions in the Nangqian Basin, Eastern Tibet: Tectonic and metallogenic implications. *LITHOS*, *246–247*, 212–227. <https://doi.org/10.1016/j.lithos.2016.01.003>
- Xu, Y., Zhu, J., Hu, R., Bi, X., Yu, H., Xu, L., et al. (2019). Heterogeneous lithospheric mantle beneath the southeastern Tibetan Plateau: Evidence from Cenozoic high-Mg potassic volcanic rocks in the Jinshajiang–Ailaoshan Cenozoic magmatic belt. *Journal of Asian Earth Sciences*, *180*, 103849. <https://doi.org/10.1016/j.jseas.2019.04.018>
- Yang, T. N., Hou, Z. Q., Wang, Y., Zhang, H. R., & Wang, Z. L. (2012). Late Paleozoic to Early Mesozoic tectonic evolution of northeast Tibet: Evidence from the Triassic composite western Jinsha–Garzê–Litang suture: Paleo-Tethyan tectonics of north-east Tibet. *Tectonics*, *31*, TC4004. <https://doi.org/10.1029/2011TC003044>
- Yang, Y., Ritzwoller, M. H., Zheng, Y., Shen, W., Levshin, A. L., & Xie, Z. (2012). A synoptic view of the distribution and connectivity of the mid-crustal low velocity zone beneath Tibet. *Journal of Geophysical Research*, *117*, B04303. <https://doi.org/10.1029/2011JB008810>
- Yang, Z., & Woolley, A. (2006). Carbonatites in China: A review. *Journal of Asian Earth Sciences*, *27*(5), 559–575. <https://doi.org/10.1016/j.jseas.2005.06.009>
- Yang, J., Xu, Z., Li, Z., Xu, X., Li, T., Ren, Y., et al. (2009). Discovery of an eclogite belt in the Lhasa Block, Tibet: A new border for Paleo-Tethys? *Journal of Asian Earth Sciences*, *34*(1), 76–89. <https://doi.org/10.1016/j.jseas.2008.04.001>
- Yin, A., Dang, Y. Q., Wang, L. C., Jiang, W. M., Zhou, S. P., Chen, X. H., et al. (2008). Cenozoic tectonic evolution of Qaidam Basin and its surrounding regions (Part 1): The southern Qilian Shan–Nan Shan thrust belt and northern Qaidam Basin. *GSA Bulletin*, *120*(7–8), 813–846. <https://doi.org/10.1130/B26180.1>
- Yin, A., & Harrison, T. M. (2000). Geologic evolution of the Himalayan–Tibetan orogen. *Annual Review of Earth and Planetary Sciences*, *28*(1), 211–280.
- Yu, X., Zhao, Z., Mo, X. X., Su, Zhu, & Wang, Y. (2003). The petrological and mineralogical characteristics of Cenozoic Kamafugite and carbonatite association in West Qinling, Gansu Province: China. *Periodico di Mineralogia*, *72*, 161–179.
- Zhang, Z., Teng, J., Romanelli, F., Braitenberg, C., Ding, Z., Zhang, X., et al. (2014). Geophysical constraints on the link between cratonization and orogeny: Evidence from the Tibetan Plateau and the North China Craton. *Earth-Science Reviews*, *130*, 1–48. <https://doi.org/10.1016/j.earscirev.2013.12.005>
- Zhao, W., Kumar, P., Mechie, J., Kind, R., Meissner, R., Wu, Z., et al. (2011). Tibetan plate overriding the Asian plate in central and northern Tibet. *Nature Geoscience*, *4*(12), 870–873. <https://doi.org/10.1038/ngeo1309>
- Zhao, J., Yuan, X., Liu, H., Kumar, P., Pei, S., Kind, R., et al. (2010). The boundary between the Indian and Asian tectonic plates below Tibet. *Proceedings of the National Academy of Sciences*, *107*(25), 11,229–11,233. <https://doi.org/10.1073/pnas.1001921107>